HELSINKI UNIVERSITY OF TECHNOLOGY
Department of Electrical and Telecommunications Engineering

Jörgen Pihlflyckt

CONTROL AND MEASUREMENT SYSTEM FOR MULTI-CHANNEL MICROWAVE RADIOMETER

Supervisor Raimo Sepponen

Instructor Martti Hallikainen

Espoo, 12th of February 2007

Foreword

This Master's Thesis was completed at the Laboratory of Space Technology at the Helsinki University of Technology. The work was conducted over many years starting as early as the summer of 1994 and forms part of the still ongoing development of the HUTRAD airborne profiling radiometer system. I would like to thank professor Martti Hallikainen for hiring me to work in the laboratory, and for offering me this opportunity to be involved in a truly exciting field of study.

I would also like to thank my colleagues, who have worked with me on the HUTRAD system over the years. Martti Toikka, Lauri Kurvonen, Esa Panula-Ontto, Tomi Tirri, Kimmo Rautiainen, Janne Lahtinen, Ilkka Mononen, Tuomo Auer, Martti Kemppinen, Pekka Rummukainen, Aleksi Aalto and Juha Lemmetyinen all have contributed in some way to my work. There are many others who have helped in som way, and my gratitude also goes to all the other laboratory staff not explicitly mentioned here. A special thanks goes to the laboratory's pilot, Simo Tauriainen, who flew the aircraft, demonstrated excellent piloting skills and safely brought us back to earth every time. Furthermore, I would like to thank Mark Woods for proofreading the manuscript, and Tom Lille for his feedback regarding the general structure of the thesis.

Finally, I would like to thank my parents and my sister and her family for supporting me and believing that I could actually pull this off, even though at times it didn't seem likely. A special thanks goes to my late deerhound, Dora, who on several occasions reminded me when it was time to take a break and go for a walk in the woods.

Last, but far from least, I would like to thank my wife, Sanna-Liisa, who devotedly has loved and cared for me in spite of the many late nights of neglect towards her during the final phase of writing this thesis.

Otaniemi, 12th of February 2007 Jörgen Pihlflyckt

HELSINKI UNIVERSITY OF TECHNOLOGY | **ABSTRACT OF THE MASTER'S THESIS**

Author: Jörgen Pihlflyckt

Name of the thesis: Control and measurement system for multi-channel microwave radiometer

Date: 12.2.2007 **Number of pages:** 68

Faculty: Department of Electrical and Communications Engineering

Professorship: S-66 Applied Electronics

Supervisor: Raimo Sepponen

Instructor: Martti Hallikainen

The Laboratory of Space Technology has built several microwave radiometers over the years, and in 1994 the laboratory purchased a used short SC7 skyvan aircraft in order to perform airborne measurements with these radiometers. The large rear door opening allowed more instruments to be fitted at the same time, and it was decided to build additional radiometer receivers in order to more completely match the frequencies of the near-future satellite microwave radiometers. To accomplish matching frequencies, new receivers were needed at frequencies 6.8 GHz, 10.65 GHz and 18.7 GHz.

This thesis describes the control and measurement system for these three new receivers. Chapter 1 briefly describes the background motivation behind the HUTRAD system, and chapter 2 contains a short theoretical introduction to different radiometer types.

The general design of the measurement system is described in chapter 3, and all the different subsystems are presented briefly at a block diagram level. The computer hardware and associated interfacing cards used are also described here. The measurement software is also briefly presented, even though the software is not part of the work of this thesis.

Chapter 4 contains the most important part of the author's work for this thesis. A special low-frequency amplifier with an integrating analog-to-digital conversion system based on a monolithic voltage-to-frequency converter chip was designed, and is described in detail here. There are also a few additional electronic circuits designed by the author described here.

The functionality tests and some measurement results are presented in chapter 5, and the conclusions from these measurements and the most important lessons learned from this work are presented in chapter 6.

Keywords: Radiometer, Measurement, Control

Table of Contents

List of Symbols

$\boldsymbol{B}$	Magnetic flux density
$\boldsymbol{B_f}$	Spectral radiation density
$\boldsymbol{c}$	The speed of light
$\boldsymbol{D}$	Electric flux density
$\boldsymbol{d_T}$	Data word as a function of temperature
$\boldsymbol{E}$	Electric field
$\boldsymbol{f}$	Frequency
$\mathbf{G}$	Gain
$\boldsymbol{H}$	Magnetic field
$\boldsymbol{h}$	Planck's constant
$\boldsymbol{I}$	Current
$\boldsymbol{I_X}$	Excitation current
$\boldsymbol{J}$	Current density
$\boldsymbol{k}$	Boltzmann's constant
$\boldsymbol{R_T}$	Thermistor resistance as a function of temperature
$\boldsymbol{R_0}$	Thermistor resistance at 0°C
$\boldsymbol{R_{d0}}$	Resistance corresponding to zero data word
$\boldsymbol{T}$	Temperature
$\boldsymbol{T_A}$	Antenna brightness temperature
$\boldsymbol{T_R}$	Receiver noise temperature
$\boldsymbol{T_N}$	Reference load brightness temperature
$\boldsymbol{t}$	Time
$\boldsymbol{U}$	Voltage
ε	Regulator error
η	Regulator output
λ	Wavelength
ρ	Electric charge density
τ	Time constant
Ω	Resistance

List of Acronyms

AMSR	Advanced Microwave Scanning Radiometer
A/D	Analog-to-Digital
AC	Alternating Current
BIOS	Basic Input-Output System
BNC	Bayonet Neill-Concelman
CMOS	Complementary Metal-Oxide-Semiconductor
CPU	Central Processing Unit
CRC	Cyclic Redundancy Checksum
CSMA/CD	Carrier Sense Multiple Access w. Collision Detection
DC	Direct Current
EEPROM	Electrically Eraseable Programmable Read-Only Memory
EMAC	European Multi-sensor Airborne Campaign
ESA	European Space Agency
GPS	Global Positioning System
HUTRAD	Helsinki University of Technology RADiometer
I/O	Input/Output
IC	Integrated Circuit
ISA	Industry Standard Architechture
LAN	Local Area Network
LF	Low Frequency
MBit/s	MegaBits per Second
MIMR	Multi-channel Imaging Microwave Radiometer
MOSFET	Metal-Oxide-Semiconductor Field-Effect-Transistor
MS-DOS	MicroSoft Disk Operating System
NTP	Network Time Protocol
PC	Personal Computer
PPM	Parts Per Million
PRT	Platinum Resistance Thermometer
PWM	Pulse-Width-Modulated
RF	Radio Frequency
RMS	Root Mean Square
TCP/IP	Transmission Control Protocol/Internet Protocol
TKK	Teknillinen KorkeaKoulu
TTL	Transistor-Transistor Logic
UDP/IP	User Datagtam Protocol/Internet Protocol
V/F	Voltage-to-Frequency
VGA	Video Graphics Array
VNA	Vector Network Analyzer

1. Introduction

1.1. Background

The Laboratory of Space Technology at the Helsinki University of Technology (TKK) started building a profiling microwave radiometer system (HUTRAD) for airborne remote sensing research purposes in 1990. The initial frequencies were 24, 34 and 48 GHz. [1] This three-channel radiometer system was successfully operated using a rented helicopter [2], and in 1991 a dual-polarized 94 GHz receiver [3] was added, giving a total of five radiometer channels.

HUTRAD was originally designed to operate at the same frequencies as the MIMR satellite instrument [4] to be built by the European Space Agency (ESA). The frequencies of the MIMR were to be 6.8, 10.65, 18.7, 23.8, 36.5 and 89 GHz, of which three were very close to the existing HUTRAD frequencies. It was decided to add three new receivers to HUTRAD, so that it would be possible to develop satellite data interpretation algorithms even before the instrument was actually launched into orbit. MIMR was never completed, but the same design goals have been has been met by the very similar AMSR-E instrument built by Mitsubishi Electric. [5]

The three new receivers, were added to the existing system in 1995, and the measurement and control system for these three receivers is the subject of this thesis. The receivers are all dual-polarized, adding a total of six new radiometer channels. At this time the 48 GHz receiver was removed from the system, because it no longer performed as expected, and the frequency was of little importance as far as the AMSR data was concerned. The 94 GHz receiver's data would be used as reference data for the 89 Ghz AMSR channel, while an additional 93 GHz dual-polarized imaging radiometer subsystem was simultaneously being developed independently. [6] At this point the total number of receiver channels had reached 12, two of which belonged to the independent imaging radiometer system.

In order to operate the complete HUTRAD system more efficiently, the laboratory purchased a used Short Skyvan SC7 [7] aircraft in 1994. The Skyvan is particularly suitable as a remote sensing platform, because of its spacious passenger cabin and large rear cargo door, which can be left open in flight. Another advantage of the skyvan is its fairly low air speed, which allows for longer data integration times, thus improving the quality of the measured data. The ten profiling channels were all operated on board the Skyvan during the European Multi-sensor Airborne Campaign (EMAC) [8] in the winter and spring of 1995.

After the EMAC campaign, the Laboratory of Space Technology decided to rebuild the original radiometer receivers because their performance was not satisfactory during the EMAC campaign. There were some linearity problems with their electronics, and the excessive cabling lengths required in the Skyvan caused interference, particularly in the 94 GHz receiver. Another problem was time synchronization of the data, and this made geographical localization of the measured data very difficult. The later version of the

radiometer system was specially designed for installation into the rear cargo door area of the Skyvan, and for remote operation via the on-board ethernet network.

1.2. Design objectives

During the EMAC campaign in 1995, it became clear that low voltage analog signals were difficult to transmit from the rear cargo area of the aircraft to the inside of the passenger cabin because of the electrically hostile environment. This meant that digitising the measured signals should be carried out as close as possible to the actual receivers, while system monitoring should be carried out inside the passenger cabin. This requirement implies utilization of some kind of airborne network, which would be used to transmit measured data and control commands. The network needed to be of a well supported type with sufficient performance. It also needed to be easy to configure and maintain with readily available hardware and software.

The measurement subsystem needed to be reliable, and provide data backup services and redundancy in case of suddenly occurring hardware failures. It was also important for significant error conditions to be easily detectable and diagnosable during ongoing measurements with the possibility to modify operating parameters in-flight in order to correct possible problems.

Last but not least, the control and measurement system needed to be easy to maintain and upgrade as new receiver channels with different requirements were added to the system. This implied that the hardware and software should be well documented, and indeed, several Master's theses have been written on the subject of HUTRAD, including this one. This thesis is dedicated to the control and measurement system of HUTRAD, and at the time of writing is the most detailed description of the overall system design. The most important design criteria are summarised in table 1.1.

Table 1.1. Measurement system design requirements

Radiometer data inputs	• 6 channels • ±0-10 mV sensitivity • At least 12-bit precision • Adjustable integration time 0.1-1 s
RF switch control	• 4 switches: ±12 volts, dual-ended • 2 switches: ±5 volts, single-ended • Programmable square-wave signal • Controlled in pairs
Temperature sensors	• 4 sensors per receiver box, total of 12 sensors • 0.1 °C measurement precision • Option for additional temperature sensors
Temperature control	• 3 independent regulators • Inputs from any of the sensors • Should be able to maintain inside temperature for more than ±10 °C environmental temperature change

2. Theory

2.1. Brightness temperature

Electromagnetic radiation is one of the fundamental physical phenomena in the universe. The behaviour and propagation mechanisms of electromagnetic radiation have been subject of much research in modern times, and it has been demonstrated that electromagnetic fields and waves can be accurately described using Maxwell's equations [9]

$$\nabla \times E = -\frac{\partial B}{\partial t} \tag{1}$$

$$\nabla \times H = J + \frac{\partial D}{\partial t} \tag{2}$$

$$\nabla \cdot D = \rho \tag{3}$$

$$\nabla \cdot B = 0 \tag{4}$$

where E is the electrical field, H is the magnetic field, D is the electric flux density and B is the magnetic flux density.

Every physical object emits and absorbs electromagnetic radiation in differing amounts depending on the surrounding temperature and the physical properties of the object in question. Some objects reflect most of the incoming radiation while others absorb incoming radiation, thus increasing their physical temperature. As the physical temperature of the object increases, it will emit an increasing amount of electromagnetic radiation until equilibrium is reached.

A perfect blackbody has a reflection coefficient equal to zero, and therefore its temperature can be reliably measured by measuring the power level of the emitted electromagnetic radiation. The emitted frequency spectrum of the radiation from a perfect blackbody depends on the temperature of the object, and can be described with Planck's radiation model [10]

$$B_f = \frac{2hf^3}{c^2} \cdot \frac{1}{e^{\left(\frac{hf}{kT}\right)} - 1} \tag{5}$$

where f is the frequency of the electromagnetic radiation. At microwave frequencies, the spectrum can be accurately approximated with Rayleigh-Jeans formula.

$$B_f = \frac{2 \cdot k \cdot T}{\lambda^2} \tag{6}$$

Neither Planck's nor Rayleigh-Jeans radiation model are exactly applicable for real physical objects, simply because they are not ideal blackbodies. The physical temperature of a perfect blackbody that would emit the same radiation power, is defined as the brightness temperature of the object.

2.2. Radiometer principle

In its simplest form, a radiometer receiver is a very sensitive microwave receiver, which estimates the brightness temperature of an object by measuring the power level of the received thermal noise. This power level consists of thermal noise emitted by the object, noise generated elsewhere which is reflected by the object and possibly other interfering signals. In addition to this, the receiver itself generates noise internally, which usually has a larger amplitude than all the other signal components put together. The only desired component is usually the noise power level from the measured object, which corresponds to its brightness temperature, while the other components should be compensated for as much as possible.

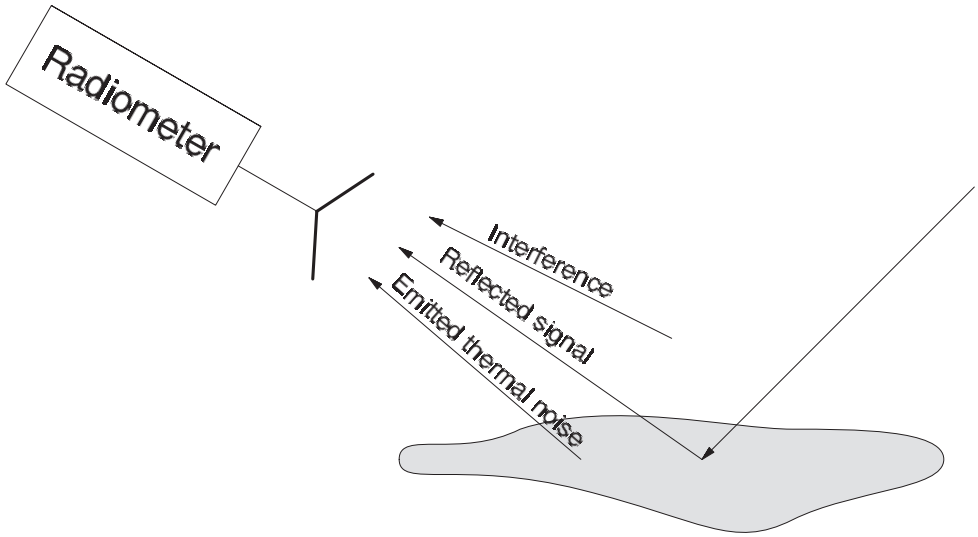

Figure 2.1: Remote sensing using a radiometer.

The unwanted reflected signal from the object under measurement can be very difficult to estimate and compensate for if the reflection properties of the measured object are not well known. The source, and therefore the properties of any reflected signals can also be very difficult to determine. There are, however, some radiometer applications that utilize the reflected signal, but in principle they should be called radar applications because

they are not necessarily passive receiver applications and usually utilize some kind of transmitter.

The noise generated in the medium between the measured object and the radiometer is usually well known, because the electrical properties of the atmosphere are well known. Moisture in the atmosphere can, however, have some influence on the measurements and introduce weather-related variations into the measured signals.

The largest contribution to the total noise power detected by the radiometer is in most cases generated by the radiometer itself, because each component in the radiometer generates additional noise. This internally generated noise from the receiver components can be compensated for if the noise temperature of the receiver is well known. In order to accomplish this, the radiometer receiver output is usually calibrated by measuring one or more well known reference targets.

2.3. Measurement accuracy

Because the useful signal is noise, and is likely to be small compared to the total noise power detected by the receiver, the signal has to be integrated a certain amount of time before the desired precision is achieved. This is usually achieved by some sort of integrating analog-to-digital conversion arrangement, possibly with software assistance. The longer the integration time is, the greater the resolution of the radiometer will be. The variance of the noise power level gets evened out over time, while the mean value stays the same as long as the measured brightness temperature stays the same. The smallest difference in brightness temperature that theoretically can be measured is [11]

$$\Delta T = \frac{T_A + T_N}{\sqrt{B \cdot \tau}} \tag{7}$$

where T_A is the brightness temperature at the radiometer input, T_N is the noise temperature of the radiometer itself, B is the bandwidth of the receiver and τ is the integration time.

Because the noise temperature of the receiver varies with the physical temperature of the receiver, it is usually important to keep at least some of the receiver components at a constant temperature. Another problem is the very slow variation of amplifier gain and noise temperature caused by component drift and aging. This very slow drift can be effectively compensated for by thoroughly calibrating the radiometer every now and then.

2.4. Different types of radiometers

2.4.1. The total power radiometer

The simplest type of radiometer receiver is the total power radiometer. The noise signal from the antenna is filtered, amplified and detected as a voltage which is proportional to the brightness temperature of the measured object.

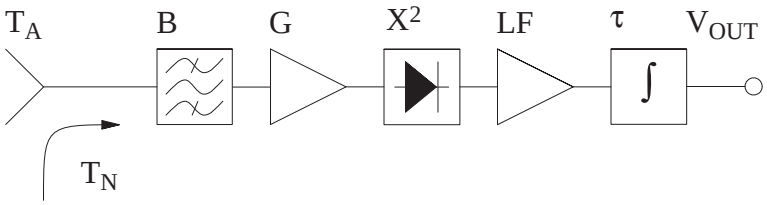

Figure 2.2: Total power radiometer block diagram.

Because the incoming noise signal is summed to the internal noise of the radiometer, the output voltage will not only depend on the measured brightness temperature, but also on the noise temperature of the receiver itself. The output voltage can be expressed as

$$V_{OUT} = c \cdot \left(T_A + T_N \right) \cdot G \tag{8}$$

where c is a constant, which depends of the combined performance of the receiver components. The total power radiometer is very sensitive to the gain and noise level fluctuations of the receiver components, and consequently must be kept at a very constant temperature. Periodic calibration during measurement might also be necessary in order to achieve the desired precision.

Another problem is, that the low frequency amplifier stage must be DC connected, which makes the LF amplifier system susceptible to long-time drift and 1/f noise. The LF amplifier is necessary, because the detector diode has to operate at power levels where its transfer function best follows the square law. This causes the detected voltage to be in the order of a few millivolts, which is problematic to handle with direct current amplifiers. Usually, some sort of chopper-stabilized DC amplifier can be used to counter these problems.

2.4.2. The Dicke radiometer

The stability problems of the total power radiometer are significantly reduced in the Dicke radiometer, where the input is switched between the antenna and a reference load at a well known temperature. [12]

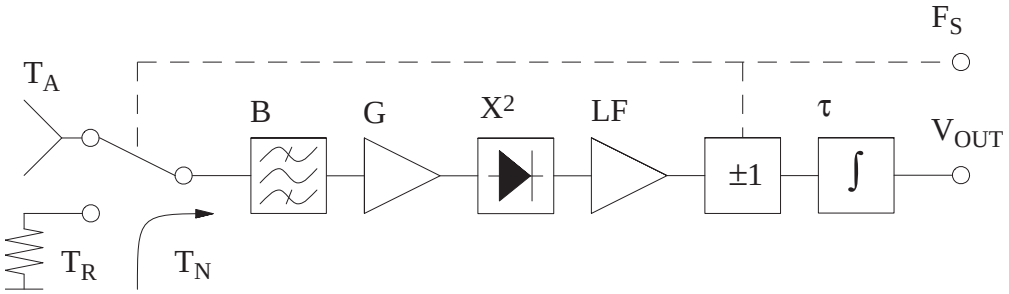

Figure 2.3: Dicke radiometer block diagram.

The signal from the antenna and the signal from the reference load are integrated at equal integration times, but with opposite signs. This effectively eliminates the noise contributed from the receiver blocks between the input switch and the synchronous detector. The output voltage dependency of the receiver noise temperature is reduced, but gain variations still affect the result.

$$V_{OUT} = c \cdot \left(T_A - T_R \right) \cdot G \tag{9}$$

The low-frequency amplifier can also be AC-connected, because the DC component is not needed any longer. This greatly improves the long-term stability of the radiometer, especially of the LF components just after the detector diode.

The sensitivity, however, is halved because the receiver is connected to the antenna only half of the time. The smallest measurable difference in brightness thus becomes:

$$\Delta T = 2 \cdot \frac{T_A + T_B}{\sqrt{B \cdot \tau}} \tag{10}$$

This is a small price to pay for a great improvement in stability. A better, but more expensive solution would be to use a four-way dicke switch connected to two separate receivers with a common antenna.

2.4.3. The noise injection radiometer

Even further stability improvement can be achieved by adding a controlled noise source to the input of a Dicke radiometer. The noise source injects an adjustabe amount of noise into the radiometer input, with the idea to keep the total noise power level constant at the radiometer input and output. [13]

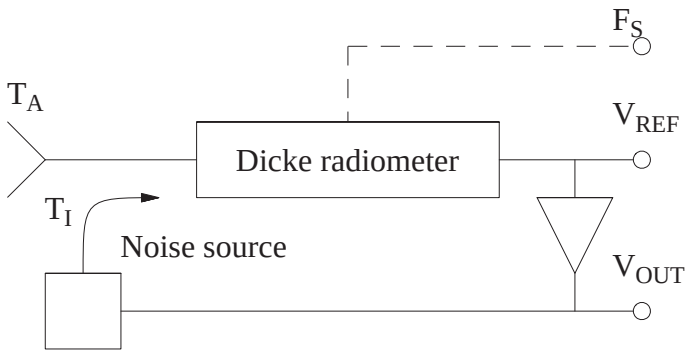

Figure 2.4: Noise injection radiometer.

The noise source is controlled by the output voltage, and the reference voltage is kept constant. The output voltage is taken from the noise source control signal, and the dependency of receiver gain and noise temperature is now fully compensated. The regulator loop is subject to the same stability criteria found in all types of regulators, and the regulator loop amplifier might need careful tuning in order to avoid oscillation.

3. General system design

3.1. The radiometer network

Because the complete system was built gradually over several years and needed to be operated both on the Skyvan aircraft and in the laboratory under different configurations, a modular design approach had to be taken. The rear cargo area on the aircraft, where the antennae and receiver units are installed were inaccessible during flight and consequently, some sort of local area network (LAN) for data transmission and system monitoring was needed.

The current network implementation built by the author is a straightforward extension to an original RS232-based remote control concept developed by Tomi Tirri. [14] Figure 3.1 shows a diagram of a typical network configuration with both the low- and high-frequency subsystems and two redundant monitoring workstations connected to the network.

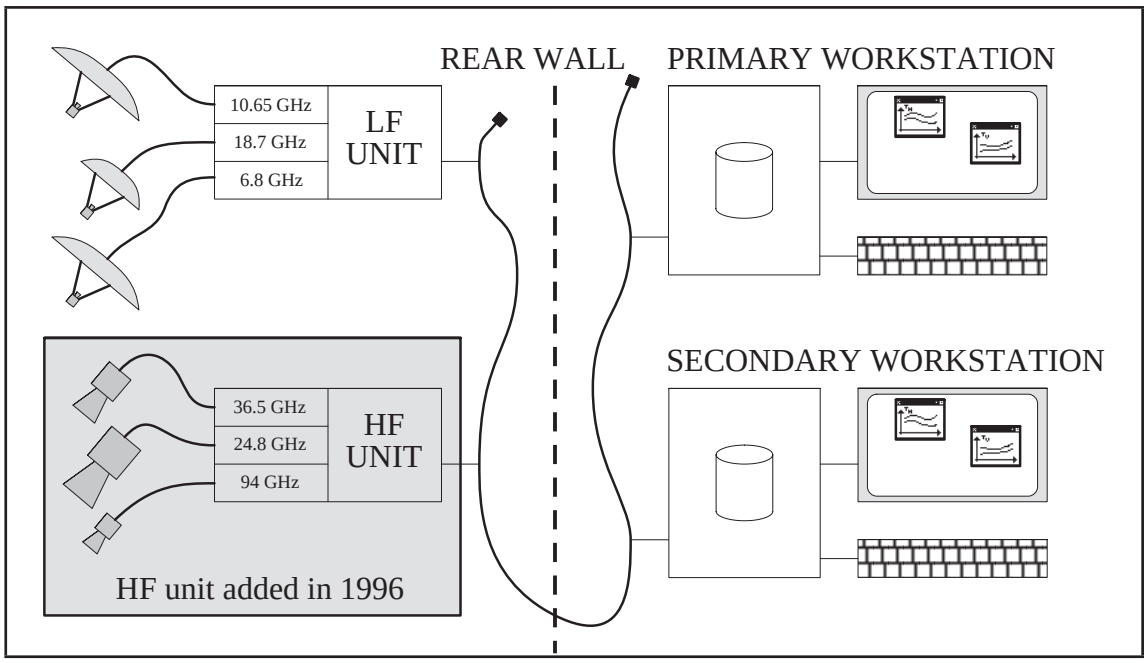

Figure 3.1: Radiometer network.

The LAN consists of standard PC networking hardware with thinwire coaxial ethernet cabling. This gives a maximum theoretical total data transfer capability slightly smaller than one megabyte per second for a network with 10 MBit/s signalling rate. The practical network bandwidth is, however, lower than this because the physical network media is shared with all the other connected stations. The behaviour of ethernet networks at varying utilization levels is a well researched subject, and is documented in several reports. [15] [16]

A single radiometer system typically produces less than five kilobytes of data even at minimal integration times, and consequently, both radiometer systems will use less than 0.1% of the theoretical network bandwidth. This is such a small amount of data, that the

effects of the radiometer data can safely be assumed to have minimal impact on total network performance. However, if the network should become heavily loaded by other network traffic, this traffic will slow down radiometer data transmission and is also likely to increase the ratio of lost data packets. An isolated private network has been built in the laboratory, in order to be able to test the radiometer network and evaluate its networking performance.

The data collected by the control processor module in the receiver unit is packed into raw ethernet data frames, and sent as such to the network hardware. The network controller hardware then adds a 2-byte CRC checksum to the data packets and send the data packet over the network cabling after verifying that the network is available. The receiving network controller automatically verifies the CRC checksum upon packet reception, and delivers the data packet to the data recording and monitoring software. The used network protocol is designed to be as simple as possible in order to minimize processing overhead and to ensure as good real-time performance as possible.

The low-level software driver interface chosen was the packet driver specification now maintained by Crynwr software. [17] The first version of the radiometer control and measurement software was written for MS-DOS, and the large library of hardware drivers available for the packet driver specification at the time was a very important reason for this decision.

Using a higher-level networking protocol such as TCP/IP or UDP/IP is theoretically safer, but experience in the laboratory has shown the reliability and performance of most TCP/IP protocol implementations for MS-DOS to be rather poor, and in some cases using UDP/IP actually has shown decreased reliability when compared to the low-level packet driver interface.

A disadvantage with the low-level packet driver interface is the potential loss of packets going undetected. Therefore, a sequence number and time stamp was added to each data packet before it was given to the packet driver. The measurement software at the receiving end checked the sequence number of the incoming data packets and made a notification of any lost packets to a log file.

The collision-detecting and retransmission mechanism (CSMA/CD) implemented in ethernet hardware also introduced a potential small random transmission delay to the data packet transmission process. In order to compensate for this, the measurement software also checed the time stamp of the incoming data packets, and a simple time synchronization protocol was implemented in order to compensate for time delays with a precision of approximately 0.1 seconds. This approximates the finest possible timing resolution when using standard PC BIOS calls and MS-DOS system calls.

3.2. The radiometer units

The receivers were grouped into two separate units, the low-frequency unit and the high-frequency unit. Both units had a control processor module, which collected data from up to eight radiometer data channels. The control processor was also able to measure up to 16 temperatures, and up to four of these could be used to regulate the physical

temperature inside the receivers. Figure 3.2. shows a logical block diagram of one complete radiometer unit with three receivers connected.

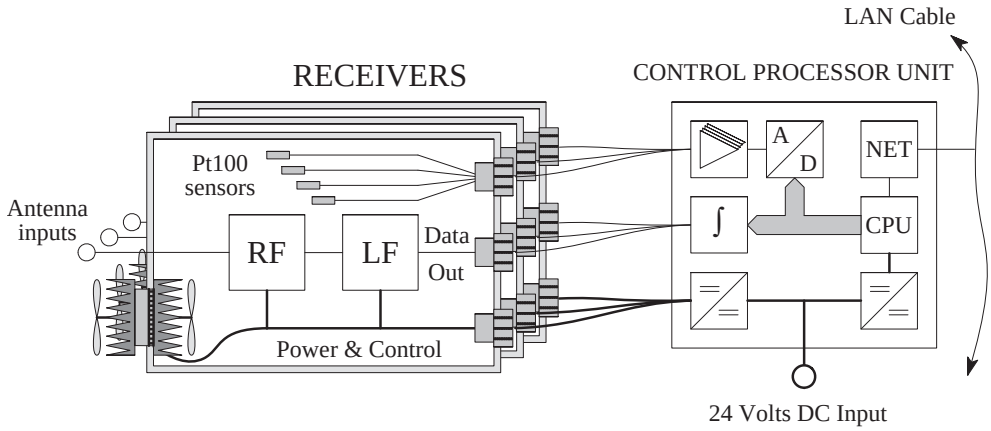

Figure 3.2: Receiver unit with three receivers connected.

As far as the measurement system is concerned, the receivers were identical in design, and only identified by their frequency and channel names. Each radiometer unit could theoretically have been operated with anything from one to up to eight receiver channels connected, but the current HUTRAD system uses only three dual-channel receivers per unit. The later added HF radiometer receiver unit is equipped with two dual-channel receivers and one four-channel receiver.

Mechanically, the complete LF unit is enclosed in a single large thermally insulated enclosure weighing a total of 85 kilograms. A photograph of the LF receiver unit installed in the rear cargo door of the skyvan is shown in figure 3.3.

Figure 3.3: The LF radiometer receiver unit.

The LF receiver unit has two 60 cm parabolic reflector dish antennae for the 6.8 GHz and the 10.65 GHz receivers, and a smaller 30 cm parabolic reflector antenna between the two larger antennae for the 18.7 GHz receiver. The topmost parabolic antenna for the 10.65 GHz receiver was not installed until some time after the unit was assembled, because at first it did not fit inside the aircraft without some small modifications to the

enclosure. The independently developed 94 GHz imaging radiometer is shown to the left in the photograph.

The large weight and size of this unit proved quite difficult to handle, and consequently the control processor unit for the HF unit built later was mounted in a separate 19 inch rack module.

3.2.1. The RF receiver components

The design and construction of the RF sections of the HUTRAD radiometer system has been thoroughly covered in the Master's thesis of Kimmo Rautiainen, [18] and is therefore not covered in detail here. A short overview here is made, however, in order to be thorough.

The low-frequency receiver unit consists of three receivers operating at 6.8, 10.65 and 18.7 GHz. The 18.7 GHz receiver is a superheterodyne receiver, while the two others are tuned radio frequency receivers. All three receivers are Dicke radiometers and have separate horizontal and vertical channels, giving a total of six channels.

The high-frequency receivers operate at 24.8, 36.5 and 94 GHz frequencies, and all three of them are superheterodyne receivers with both horizontal and vertical channels. The 94 GHz receiver is a total power radiometer, while the two other receivers are Dicke radiometers. The 36.5 GHz receiver also has two additional analog cross-correlated channels, thus giving a total of eight channels in the high-frequency receiver unit. The cross-correlated channels are described and analysed in the Masters thesis of Janne Lahtinen. [19]

3.2.2. The LF amplifier components

The design and manufacture of the low-frequency circuitry and the control processor unit of the lower-frequency unit of the HUTRAD radiometer system is the main subject of this thesis, and is briefly explained at block diagram detail level below. A more detailed explanation of the LF circuit functions can be found in the next chapter of this thesis.

The maximum signal output level from the square-law detector diode is in the order of a few millivolts, and a sensitive low frequency amplifier is needed before the signal can be properly digitised. The amplifier circuit is designed as a general-purpose radiometer amplifier so that the same amplifier design can be used for all the receivers in the HUTRAD system. There are, however, a few improvements made only to the newer version of the LF amplifiers used in the high-frequency radiometer unit. These are only minor changes, such as a newer operational amplifier types and additional buffer circuits integrated together with two LF amplifiers on the same circuit board. These improvements were made by Mr. Ilkka Mononen, and this thesis documents the older version, although the circuit diagrams presented in the next chapter are very similar to the new improved version.

The mode of operation (Dicke- or total power mode) is selected with SW2 by a static logic signal from the control processor. The LF amplifier circuit also contains the phase

inverter and synchronous detector switch SW1 needed for the Dicke radiometers. Both switches are implemented using CMOS analog switch circuits.

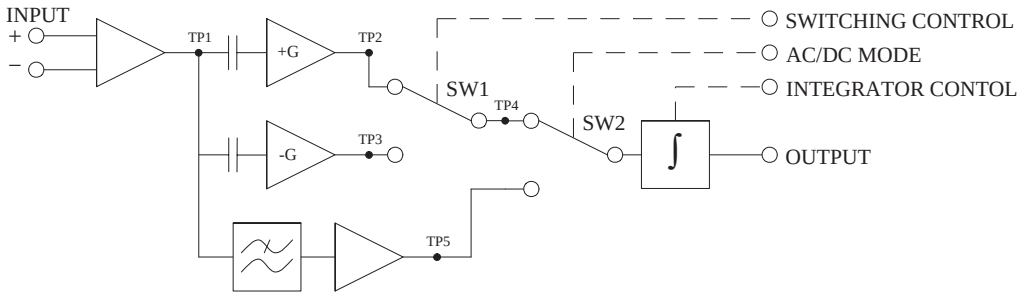

Figure 3.4: LF Amplifier block diagram.

The incoming LF signal is first fed through a buffering instrumentation preamplifier, and is then divided into three separate signal paths. The first two signal paths are AC-connected and have equal gains, but with opposite signs. When operating as a Dicke radiometer, the signal output is switched between these two signal paths synchronously with the Dicke switch at the antenna input.

The third signal path is low-pass filtered and DC-connected and is only to be operated if the corresponding radiometer receiver lacks a Dicke switch like the 94 GHz radiometer, or if the Dicke switch has malfunctioned for some reason. This signal path is selected by changing the state of SW2, and is programmed statically by the control processor or hardwired to a given logic level according to radiometer type.

The synchronous detector consists of the two opposite-signed amplifier signal paths and the analog switch SW1. The following waveform example illustrates how the synchronous detector works.

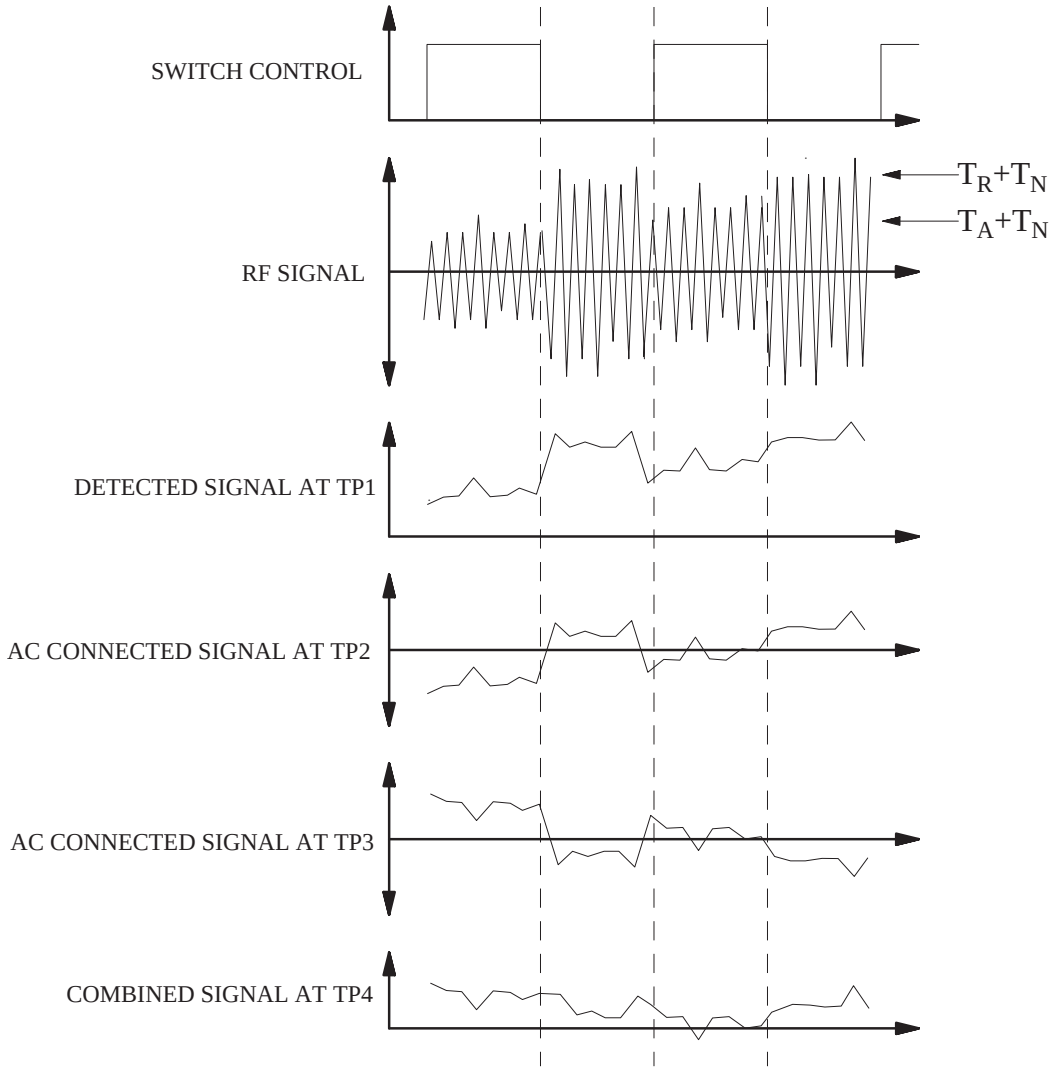

Figure 3.5: Expected signal waveforms.

Typically, the measured brightness temperature T_A is smaller than the temperature of the reference load T_R, giving a lower power level of the noise signal when the input is connected to the antenna. When this RF signal is detected by an envelope detector, the signal at test point TP1 results. This signal is heavily influenced by the noise temperature T_N of the RF components and 1/f-noise and drift of the LF components. To counter these problems, the signal is split into two AC-connected amplifier stages. One inverting, and one non-inverting. The output signal is switched between these two signal paths synchronously with the Dicke switch, and after integration we get a voltage level proportional to the difference between the brightness temperature at the antenna, and the temperature of the reference load. When operating as a Dicke radiometer, all of the amplifier stages are thus, effectively chopper-stabilised.

3.2.3. Integrating A/D converter system

The analog signal needs to be integrated at a certain time interval, which depends on the flight altitude and ground speed. Sometimes it is necessary to change the integration time during measurement, and therefore, the integration time should be programmatically controlled and easy to change during flight. Typical integration times during

airborne measurements are in the range from 0.2 to 1.0 seconds, while ground-based measurements usually require integration times of several seconds or sometimes even several minutes.

There are many ways to achieve adjustable data integration, and use of a voltage-to-frequency converter combined with a digital counter has been chosen for the HUTRAD measurement system. The laboratory has some good experiences with this arrangement from the earlier radiometers, which were replaced by the system described here. A monolithic voltage-to-frequency converter IC can be used for a number of different analog computing purposes [20] and in this case, we can achieve integration and analog-to-digital conversion at the same time.

Low-cost integrated circuits and computer peripheral cards are readily available, and the integrator was implemented with as much readily available components as possible. It's also easy to implement optically isolated data transmission with a minimum of external components using this technique. The voltage-to-frequency converter is connected to the LF amplifier output at SW2, and produces a signal with constant amplitude and a frequency proportional to the input voltage. This signal is transmitted through the data transmission line to the control processor module via an optocoupler. The rest of the integrator system, including the counters and the integration timer is physically located inside the control processor module itself.

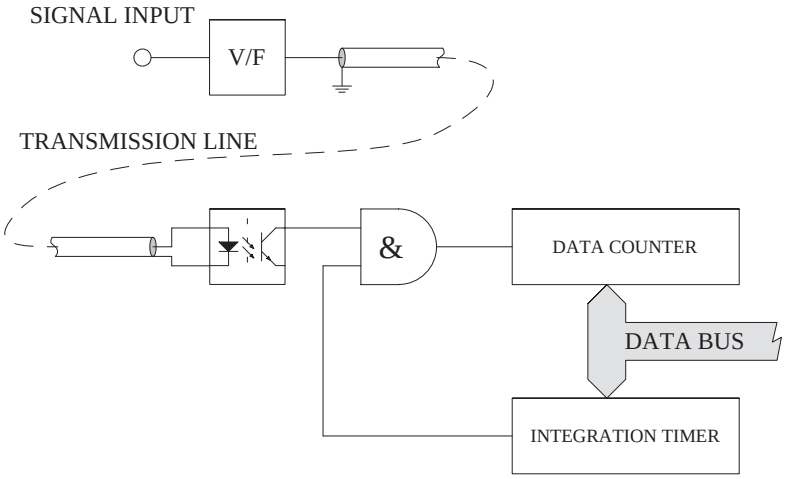

Figure 3.6: Integrating A/D-converter system.

Note that the signal present in the transmission line is not yet digitized in the time domain, even though the amplitude of the signal is discrete. Because of this, the signal can easily be transferred through a single transmission line because no clocking and bit synchronization is needed. Optical isolation of the signal eliminates interference from the receivers generated by the processor module, and allows the signal connectors to be safely hot-plugged without turning off the power to the receivers or the control processor unit.

The frequency of the signal in the transmission line is measured by a 16-bit pulse counter, which is periodically read and cleared by the control processor. The integration time is controlled by a retriggerable integration timer which controls the AND gate before the data counter. This arrangement ensures that the integration time is always correct, even if the control processor should happen to miss the end of the integration cycle due to

excessive processor load or interrupt latency. The disadvantage is that data integration is suspended for the duration of the read-and-clear operation, thus resulting in a small amount of "dead time" for the integrator. The dead time could be eliminated by an arrangement using dual counters and alternation between these. The dead time is only a small fraction of the integration time, and it was decided that the additional cost and complexity would not justify implementing this double-buffer scheme.

It is important that the data is read from the integration counter as soon as possible after the integration period has ended, because data integration cannot be resumed before the integration timer is retriggered. A rough estimate suggests, that the "dead time" typically would be in the order of a few milliseconds, which can be considered small when compared to a typical integration time of 500 ms. This also means that the data samples will have a time interval between them that is slightly larger than the selected integration time. The asynchronous nature of the data is, however, not an issue, because the GPS receiver used for geolocating the data runs asynchronously with regard to the radiometers in any case.

3.3. The control processor unit

The control processor unit is built around an Ampro 486-SLC/50 embedded PC processor board equipped with a Cyrix 386-compatible CPU. This is a compact rugged processor card capable of booting MS-DOS directly from EEPROM memory without the need for traditional magnetic mass storage media. The processor is running MS-DOS, a minimal Novell Netware client, and a control and a measurement program written by the HUTRAD development team.

The control processor board is equipped with a PC/104 bus, [21] which is basically compatible with the standard PC ISA bus. Although very similar in principle, the PC/104 bus has a different electrical connector and reduced current drive capability in order to reduce the power consumption of the processor board. The I/O interface cards are mounted on the processor card as a stack and the PC/104 bus runs through the stack as shown in the figure 3.7.

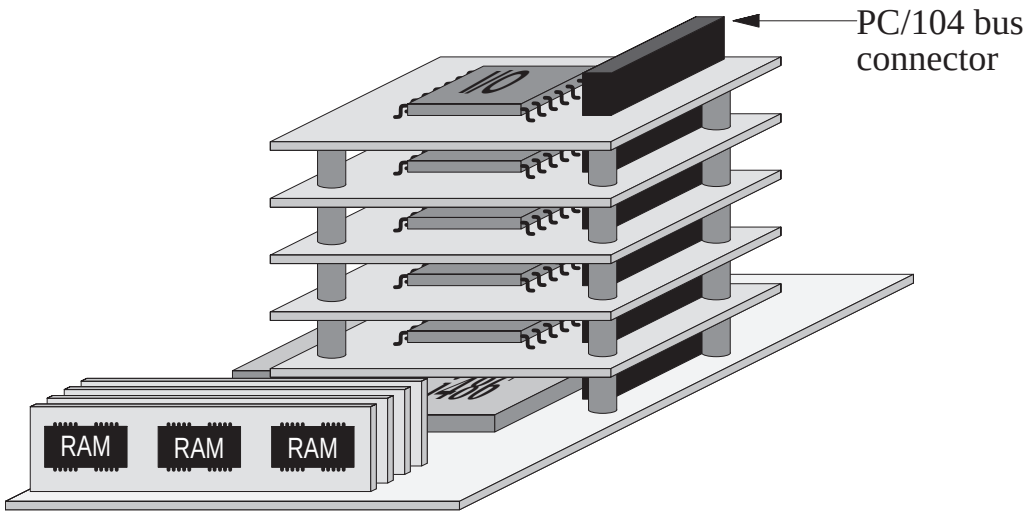

Figure 3.7: PC/104 Mechanical arrangement.

From a software point of view, the control processor module is quite similar to a standard desktop PC, and this allows the developer to use the same programming tools for software development as on a normal desktop PC. It's also possible to use any standard PC operating system with associated tools as the platform for software development. The measurement software for the control processor is copied into a bootable floppy disk image, which in turn is programmed into the boot EEPROM on the processor board.

During development and testing, the control processor unit had a standard PC keyboard and VGA display connected in order to allow easier debugging and testing. When HUTRAD is operated on the Skyvan, monitoring and control commands are given via the network from one of the monitoring workstations.

The control processor unit also contains signal conditioning electronic cards and power supplies for the processor unit itself and the radiometer receivers. Everything is installed inside a standard 19-inch industry rack module, and the only external connectors necessary to operate the radiometer unit are the 24 volts DC power input and the ethernet network BNC connector.

Interfacing the radiometers to the processor board is accomplished with two DM804 [22] counter cards, and one ANDI-MM [23] multi-purpose analog and digital I/O card. The two counter cards are each equipped with an Am9513 [24] five-channel counter chip, giving a total of 10 16-bit counters. One of the counters is dedicated for the Dicke switching frequency, and another counter channel is the data integration timer, leaving 8 channels available as radiometer data integrators. All other input and output is handled through the ANDI-MM card.

3.3.1. Receiver temperature measurement

The performance of the RF components is strongly dependent on their physical temperature, and as a consequence, their temperature should be kept as constant as possible during measurement. In order to achieve the desired radiometric sensitivity, the receivers must also be calibrated with the same inside temperatures as those used during

measurement. The calibration procedure involves large containers filled with liquid nitrogen, and the calibration procedure cannot be carried out during flight. The surrounding temperature can vary more than ten degrees and sometimes even more between ground level and flight altitude, and some kind of active temperature control system is required to compensate for this difference.

Each receiver has four temperature sensors placed at different locations, so that a constant temperature inside the receiver can be maintained. The temperature inside each receiver is actively stabilized by a Peltier [25] thermoelectric heat pump with fans attached to both sides. The fans are necessary in order to achieve sufficient thermal contact between the Peltier element and the surrounding air, and also in order to maintain sufficient air flow within the receiver housing. The air flow will decrease temperature gradients inside the receivers caused by variations in the air flow outside the radiometer enclosure.

The temperature measurement system is implemented using platinum resistive thermometer (PRT) Pt100-type devices [26] connected to four commercially available instrumentation preamplifier ANDI-RTD cards. [27] The four preamplifier cards are each connected to one of four inputs of the ANDI-MM card at the control processor bus, which in turn digitizes the analog signals. Each of the preamplifier cards have four multiplexed inputs, thus giving a total of sixteen temperature measurement channels in the control processor unit. Figure 3.7. shows the principle of one temperature measurement channel.

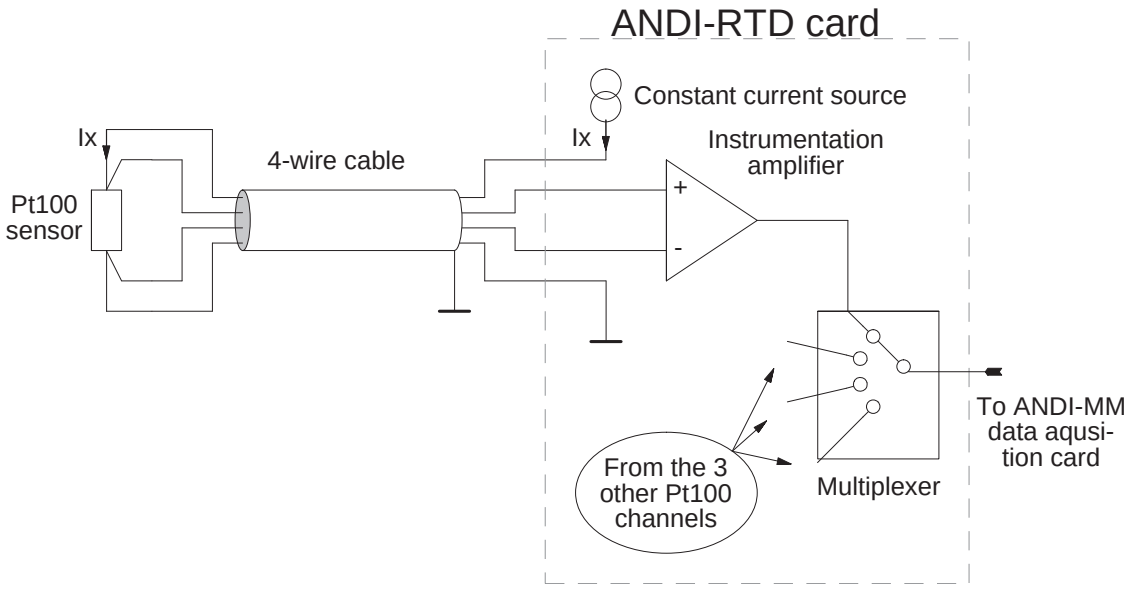

Figure 3.8: One temperature sensor channel.

A constant excitation current of 100 μA is sent through the sensor, producing a voltage across the terminals of the sensor

$$U = R_T \cdot I_X \qquad \text{(I)}$$

where R_T is the resistance of the temperature sensor and I_X is the excitation current from the constant current source. The resistance of a Pt100 sensor is only 100 Ω at zero degrees, so the resistance of the measurement cable is likely to have an impact on the

measurement if the cable is not very short. The ANDI-RTD preamplifier card inputs have separate terminals for the excitation current and the voltage measurement input, and this allows the voltage to be sampled directly from the temperature sensor terminals. The preamplifier has a large input impedance, and draws very little input current compared to the excitation current. This effectively prevents the resistance of the measurement cables from affecting the temperature measurement.

The output voltage from the ANDI-RTD card is digitised by the ANDI-MM card, and the result is a 16-bit unsigned data word, which is linearly dependent of the sensor resistance. Each of the temperature sensor measurement channels has slightly different gains and offset voltages, and in order to achieve sufficient measurement precision they must all be individually calibrated. By measuring two precisely known resistors, the gain and offset for each channel can be calculated using a straight calibration line drawn through the two calibration points.

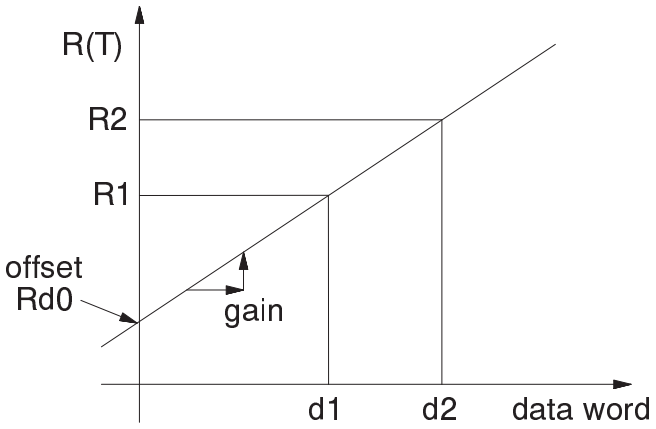

Figure 3.9: Temperature sensor channel calibration line.

The sensor resistance at the two calibration points can be expressed as a function of the measured raw data, the gain and offset of the temperature sensor channel as

$$R_1 = R_{d0} + G \cdot d_1 \tag{11}$$

$$R_2 = R_{d0} + G \cdot d_2 \tag{12}$$

where G is the gain of the temperature sensor channel. By measuring two precisely known calibration resistors and recording the raw data for each, the offset and gain can be solved as

$$G = \frac{R_2 - R_1}{d_2 - d_1} \tag{13}$$

$$R_{d0} = R_1 - G \cdot d_1 \tag{14}$$

When the gain is known, the offset can also be calculated, and the temperature sensor resistance can be calculated as a function of the raw data word as

$$R_T = R_{d0} + G \cdot d_T \tag{15}$$

Note that the offset, gain and measured data need not necessarily be expressed in proper scientific units, as long as they are used consistently throughout the calibration process. In practice, knowledge of the actual voltages at the ANDI-MM card input is irrelevant, as long as the input is not saturated at any temperature that normally occurs during measurement.

The calibration procedure theoretically needs to be performed only once, when building the radiometer units. Practice has shown, however, that every time a failing temperature sensor is replaced or the control processor module is disassembled for some reason, it is a good idea to repeat the temperature sensor calibration procedure.

The resistance of a Pt100 sensor is defined as 100 Ω at 0°C, and increases by approximately 0.385 Ω for each degree of temperature. [28] A more exact value for the sensor resistance as a function of temperature can be calculated from the Callendar-Van Dusen equation [29]

$$R_T = R_0 \cdot \left[1 + AT + BT^2 + CT^3 \cdot \left(T - 100 \right) \right] \qquad -200°\mathrm{C} < T < 0°\mathrm{C} \tag{16}$$

$$R_T = R_0 \cdot \left[1 + AT + BT^2 \right] \qquad 0°\mathrm{C} \le T < 850°\mathrm{C} \tag{17}$$

$$A = 3.9083 \times 10^{-3}\ °C^{-1} \tag{18}$$

$$B = -5.775 \times 10^{-7}\ °C^{-2} \tag{19}$$

$$C = -4.183 \times 10^{-12}\ °C^{-3} \tag{20}$$

where R_0 is the standardised resistance of 100 Ω at zero degrees. The values for A, B and C used here, are as specified in the standard, but they may also be different for certain types of temperature sensors. Since constants B and C are small compared to A, the temperature dependency may be assumed to be linear near room temperature if limited measurement precision is sufficient.

Solving the temperature from the Callendar-Van Dusen equation is difficult, because the equation is a cubic polynomial at temperatures below zero, and cubic equations are difficult, although quite possible to solve analytically. At temperatures above zero, the equation is quadratic, and can be solved as

$$T = \frac{-A \pm \sqrt{A^2 - 4B\left(1 - \frac{R_T}{R_0}\right)}}{2B} \tag{21}$$

This theoretical analysis had not been completed when the radiometers were built, and calculating a square root for each temperature sensor measured would have been too processor intensive for the rather limited performance of the control processor at the time.

Instead of using this equation, solving the sensor temperature from the measured resistance has been implemented using a look-up table from the standard and with linear interpolation between two adjacent known resistance and temperature value pairs. This introduces a small error in the temperature measurement, but the error is much smaller than the guaranteed precision of commercial grade Pt100 sensors and can thus be safely ignored.

3.3.2. Receiver temperature control

The temperature is regulated by a PI-regulator implemented in software similar to the regulator used in the 93 GHz imaging radiometer. [30] The building blocks of one temperature regulator are shown in figure 3.10. where the parts implemented in hardware and in software are separated by a dashed line.

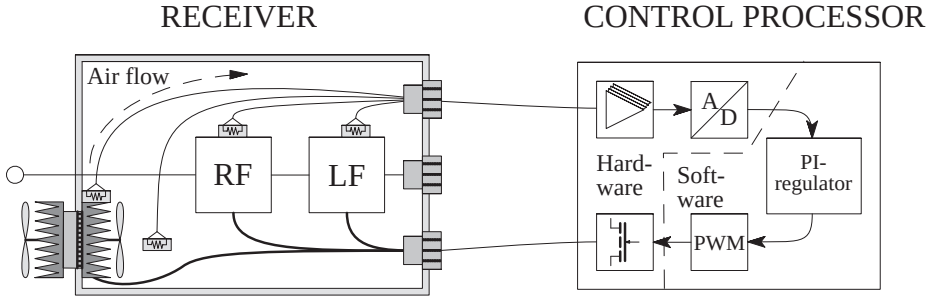

Figure 3.10: The temperature control system principle.

One radiometer unit can run up to four temperature regulators in parallel, and the regulators may be individually controlled and tuned. The input to each of the regulators may be arbitrarily chosen as any of the 16 temperature sensor channels. The regulator algorithm is a discrete implementation of a generic PI-regulator [31]

$$\eta = P\varepsilon + I\int\varepsilon \tag{22}$$

where η is the regulator output and ε is the temperature error. The generic digital PI-regulator implementation becomes

$$\eta_n = P\varepsilon_n + I\sum_{i=0}^{n}\varepsilon_i \tag{23}$$

This equation is not well suited to direct software implementation because the number of terms in the sum increases by one for each iteration by the regulator. It is also possible that if the error term is large for a long time, the sum will cause an arithmetic

overflow error in the control processor and cause the regulator to fail if special care is not taken. We can eliminate the sum by taking the difference between two consecutive regulator output values.

$$\eta_n - \eta_{n-1} = P\left(\varepsilon_n - \varepsilon_{n-1}\right) + I\left(\sum_{i=0}^{n}\varepsilon_i - \sum_{i=0}^{n-1}\varepsilon_i\right) \tag{24}$$

The two sums can be reduced to a single term, and we can express the regulator output as a function of the regulator output from the previous regulator loop iteration.

$$\eta_n = \eta_{n-1} + P\left(\varepsilon_n - \varepsilon_{n-1}\right) + I\varepsilon_n \tag{25}$$

The P and I terms are configured in software, and must be individually tuned for each of the receivers. Tuning can be accomplished by measuring the step response of each regulator and calculating proper coefficients from the result, but this has not yet been done at the time of writing. In stead, the regulator parameters have been tuned experimentally, and the results so far have been largely satisfactory.

Each regulator output is fed to a pulse-width modulator (PWM) implemented in software. The PWM modulators run asynchronously from the regulator loops as a background thread in an MS-DOS hardware interrupt handler. This guarantees that the power setting is not influenced by processor load, even if the regulator loop may run more slowly at high processor loads.

The pulse-width modulators each drive a power MOSFET bridge. The output voltage of the bridge can be reversed, and because Peltier elements are symmetric with regards to their polarity, heat can be pumped both in and out from the receiver boxes. The thermal efficiency for a Peltier element is very different for heating and cooling, and the regulator loop has separate tuning parameters for these two cases.

3.3.3. System control

All the receivers except the 94 GHz total power radiometer, need two control signals in order to operate correctly. The most important signal is the Dicke switch control frequency, which also controls the synchronous detector in the LF amplifier. This frequency must be stable, and is generated by a dedicated counter channel on one of the DM804 timer/counter cards.

The other control signal is the static AC/DC signal path selection signal, which must be properly set according to the radiometer type. This control signal rarely needs to be changed, and is in fact permanently hardwired on some of the receivers.

3.4. The monitoring workstations

The monitoring workstations are standard Linux® workstations, running on rack-mounted PC hardware. In addition to interactive user services, they offer multi-protocol file sharing network services and time synchronization services to the radiometer units, and possibly to other connected instruments as well.

Each of the workstations can be assigned as the master controller at any time, and the data can also be backed up from one workstation to any of the other workstations. Direct mirroring of the data can be achieved by sending the data packets to a multicast network address [32] so that it may be received by several network nodes at the same time without additional processing overhead.

When using several different remote sensing instruments, their data must often be analysed together and accurately cross-referenced. For this purpose, one of the workstations has a differential corrected GPS receiver board installed, and GPS positioning information may be stored on disk together with very precise timing information. The GPS receiver also acts as the primary timing source for the network synchronization protocol.

Precise clock synchronization between the workstations and instruments is implemented with the network time protocol. (NTP) The time synchronisation can achieve sub-millisecond precision, [33] and is used to synchronise the monitoring workstations with GPS time. The radiometer units use the Novell Netware protocol for initial time synchronisation, and they continuously correct their individual clock drift using a custom-built simple timing protocol.

One of the workstations can also display a digital map of the measurement site, and the geographical location of the aircraft can be shown on the map in real-time. The chosen measurement coordinates shown on the digital map can also be viewed and edited using a mouse or trackball in-flight. Changes to the measurement coordinates can be stored on the file server, and transmitted directly to the aircraft pilots over the local-area network.

3.5. Measurement software

The measurement software was written by several people over the years, and depends on several other software packages in order to work. Much of the software is not part of the work of this thesis, and the software architecture is only briefly presented here. The principal parts of the software components and their dependencies are shown in figure 3.11. The shaded software components are written by the author for this thesis.

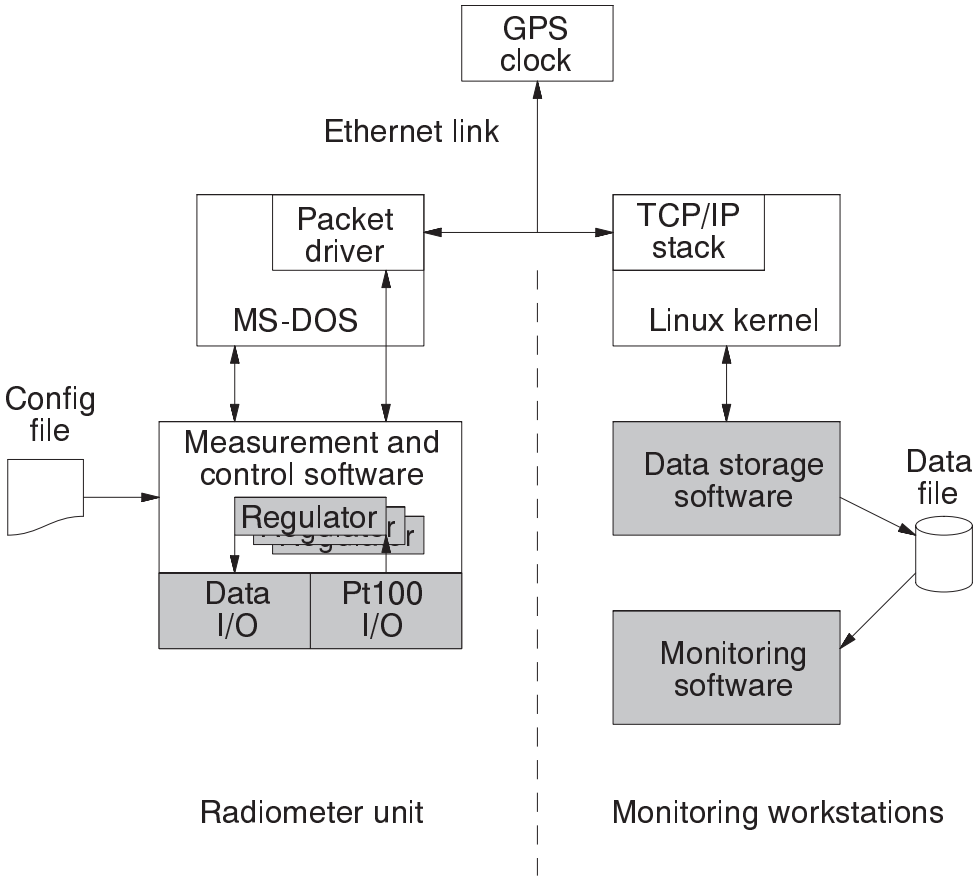

Figure 3.11: Measurement software components.

The data packets from the radiometer units are received and stored into a data file by a server process running in the workstation assigned as the master controller. The server process also verifies the time stamps and sequence numbers of each data packet, and any discrepancies are recorded into the system log. If the time stamp of a data packet is only slightly wrong, the corresponding radiometer unit is sent a time adjustment command.

The validity of the measured data can also be checked in-flight, and a simple monitoring program has been written for this purpose. The monitoring program supports simultaneous monitoring of all radiometer channels and physical temperature sensors at the same time, giving a grand total of 14 radiometer channels and 32 temperature sensors. The brightness temperature of each radiometer channel is displayed graphically as a function of time.

4. Electronic circuit details

4.1. LF amplifier

The voltage output from the RF detector diode in the receiver is in the order of a few millivolts, and needs to be properly amplified before it can be further processed. A special LF amplifier circuit which is described below, has been designed by the author for this purpose. The requirements for the LF amplifier were not precisely known in advance, and several prototypes were built in order to verify the design criteria of the final design, which is summarised in table 4.6. at the end of this section.

The LF amplifier circuit is a general-purpose amplifier designed for use in all of the profiling radiometers in the HUTRAD system. It is equipped with both AC connected and DC connected signal paths. The DC connected signal path is lowpass-filtered and is equipped with a potentiometer for DC voltage offset adjustment.

The operational amplifiers used in the LF amplifier are dual low-noise amplifiers of the type XR-5533 from EXAR. It is a direct replacement for the more common NE5533 by Philips Semiconductor. [34] The NE5533 operational amplifier requires a small external compensation capacitor in order to be stable, and the value of the capacitor may be tuned in order to optimise the frequency response of the amplifier. The circuit diagram of the LF amplifier is shown in figure 4.1.

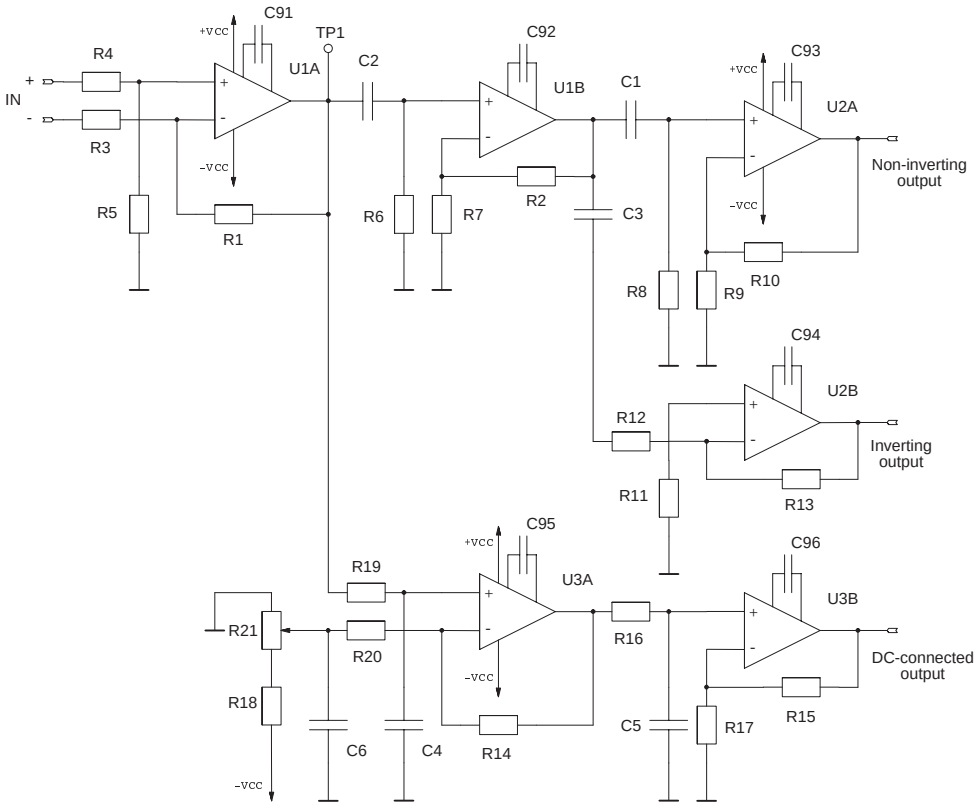

Figure 4.1. LF amplifier circuit diagram.

4.1.1. The instrumentation preamplifier stage

The first amplifier stage is the most critical component in the LF amplifier, and should have the highest precision and the lowest noise in the LF amplifier chain. The operational amplifier type chosen is a low-noise amplifier and has been connected as a differential amplifier in order to eliminate any common mode interference injected via the RF cabling and the grounding plane in the receiver.

The first amplifier stage, implemented with U1A, is a simple differential amplifier [35] with a dual-ended input. The positive input terminal is connected to the output of the RF detector diode, and the negative input terminal is connected to a grounding point very close to the detector diode. This allows the LF signal to be sampled directly at the detector diode output, and effectively eliminates interference injected via the cabling and ground plane of the RF components.

Table 4.1. U1A amplifier component values

	6.8 GHz	**10.65 GHz**	**18.7 GHz**
R1	47.5 kΩ	100 kΩ	47.5 kΩ
R3	10 kΩ	10 kΩ	10 kΩ
R4	10 kΩ	10 kΩ	10 kΩ
R5	47.5 kΩ	100 kΩ	47.5 kΩ
C91	33 pF	33 pF	22 pF

Assuming that the operational amplifier is ideal, i.e. has zero input current and infinite voltage gain, the voltage difference between the inputs will be driven towards zero via the feedback network. Resistors R4 and R5 are connected as a voltage divider at the positive input, while R3 and R1 make up the feedback network. The voltages at the operational amplifier inputs become

$$U_{OpAmpIn+} = \frac{R4+R5}{R5} U_{IN+} \tag{26}$$

$$U_{OpAmpIn-} = \frac{R3 \cdot U_{OUT} + R1 \cdot U_{IN-}}{R1+R3} \tag{27}$$

Since the operational amplifier drives these voltages towards each other, we can assume that $U_{OpAmpIn+} = U_{OpAmpIn-}$ and solve for U_{OUT}

$$U_{OUT} = \frac{R1+R3}{R3}\left(U_{IN+} \cdot \frac{R5}{R4+R5} - U_{IN-} \cdot \frac{R1}{R1+R3}\right) \tag{28}$$

In order to fully balance the inputs we choose $R_1 = R_5$ and $R_3 = R_4$ and by eliminating R4 and R5 from the equation it can be simplified as

$$U_{OUT} = \frac{R1}{R3}\left(U_{IN+} - U_{IN-}\right) \tag{29}$$

R3 and R4 are chosen as approximately 10 kΩ in order to give the amplifier an input impedance considerably larger than 1 kΩ, which is the assumed output impedance of the RF detector diode. The first amplifier stage is the only common part of the three different signal paths, and is therefore the best choice for tuning when overall LF amplifier gain is adjusted.

The voltage gain in this first stage has been tuned to 10 in the 10.65 GHz receiver, and to approximately 5 in the other receivers. The overall LF amplifier gain needs to be higher in the 10.65 GHz receiver, because the RF components in this receiver have lower gain and consequently deliver a signal with a smaller voltage to the input of the LF amplifier in this receiver.

The capacitance of C91 is 22 pF in the 18.7 GHz receiver, as recommended in the operational amplifier data sheet. In the other receivers, C91 has been increased to 33 pF in order to decrease the gain bandwidth of the amplifier. This slightly reduces the amount of high-frequency noise passing through, thus decreasing the probability of signal clipping and glitches in the final stages of the LF amplifier.

4.1.2. The AC connected signal path

In a Dicke radiometer, the entire LF amplifier chain should be AC connected in order to be as immune as possible to 1/f-noise and variations in the DC offset voltage caused by component drift and aging. The LF amplifier circuit designed for this thesis is designed with this in mind by including an AC connected signal branch to be used when the LF amplifier is used in a Dicke radiometer.

After the first amplifier stage, the LF amplifier splits the signal into two separate signal paths, one AC connected and one DC connected. The DC connected signal path is used only in total power radiometers, but may also be used temporarily in other radiometers, for instance if the Dicke switch fails for some reason.

Table 4.2. U1B amplifier component values

	6.8 GHz	**10.65 GHz**	**18.7 GHz**
R2	1 MΩ	1 MΩ	1 MΩ
R7	47.5 kΩ	20 kΩ	47.5 kΩ
R6	47.5 kΩ	20 kΩ	47.5 kΩ
C2	1 µF	1 µF	1 µF
C92	33 pF	33 pF	22 pF

The first amplifier stage in the AC connected signal path is implemented with operational amplifier U1B, and is a non-inverting amplifier, where the gain can be expressed as [36]

$$G_{U1B} = \frac{R2 + R7}{R7} \tag{30}$$

The voltage gain for U1B is as high as 51 for the 10.65 GHz radiometer due to its lower RF section gain and is tuned to approximately 22 for the other radiometers. R6 at the positive input is chosen equal to R7 in order to compensate for the input bias current of the operational amplifier. [37] R6 is also part of the first-order highpass filter between the first and second amplifier stages. The -3dB cutoff frequency of the filter is [38]

$$f_{-3dB} = \frac{1}{2\pi(R6 \cdot C2)} \tag{31}$$

The frequency response of the filter has a slope of -6 dB per octave, and a -3dB cutoff frequency of 8 Hz for the 10.65 GHz radiometer and 3.4 Hz for the other radiometers. The different cutoff frequency for the 10.65 GHz receiver is not a design criteria, but a consequence of the different resistance values in the feedback network resistors R6 and R7. In any case, the cutoff frequency is much lower than a typical Dicke-switching frequency of 1 kHz, and the square-wave modulated noise signal can be assumed to pass through with minimal distortion. The compensation capacitance used in U1B is the same as in the instrumentation preamplifier stage, U1A.

4.1.3. The non-inverting signal path

The final stage of the LF amplifier should deliver a signal suitable for the digitising system used in the radiometer. The amplitude of the signal should be as large as possible, but not exceed the input capabilities of the digitising system. Equally the signal should not be clipped or distorted in any way. The final amplifier stage in the non-inverting signal path also implements the signal branch with a positive sign in the synchronous detector needed in a Dicke radiometer.

After the second amplifier stage, the AC connected signal path is further split into two separate signal paths. The AC connected signal is fed to one inverting final amplifier stage, implemented with U2A, and one non-inverting final amplifier stage, implemented with U2B. These two signal paths should have equal gains, but reversed polarities.

Table 4.3. U2A amplifier component values

	6.8 GHz	**10.65 GHz**	**18.7 GHz**
R8	47.5 kΩ	51.1 kΩ	47.5 kΩ
R9	46.4 kΩ	47.5 kΩ	46.4 kΩ
R10	1 MΩ	1 MΩ	1 MΩ
C1	1 µF	1 µF	1 µF
C93	33 pF	47 pF	22 pF

U2A is functionally equivalent to U1B, with the exception of the design characteristics used in the 10.65 GHz radiometer. The gain for the final non-inverting amplifier stage, U2A can be calculated using

$$G_{U2A} = \frac{R10 + R9}{R9} \tag{32}$$

in the same way as for U1B, and is approximately 20 for all the receivers. R8 is chosen to balance the resistance of R9 and R10 when connected in parallel, in order to compensate for the input offset current of the operational amplifier U2A. C1 and R8 are a first-order lowpass filter with a cutoff frequency of approximately 3.4 Hz.

4.1.4. The inverting signal path

The final amplifier stage in the inverting signal path of the LF amplifier has equal design criteria as the non-inverting signal path, but with opposite polarity. It implements the signal branch with negative sign in the synchronous detector in a Dicke radiometer.

The final amplifier stage in the inverting signal path is implemented as an AC connected inverting operational amplifier using U2B.

Table 4.4. U2A and U2B amplifier component values

	6.8 GHz	**10.65 GHz**	**18.7 GHz**
R11	47.5 kΩ	51.1 kΩ	47.5 kΩ
R12	47.5 kΩ	51.1 kΩ	47.5 kΩ
R13	1 MΩ	1 MΩ	1 MΩ
C3	1 µF	1 µF	1 µF
C94	33 pF	47 pF	22 pF

The gain of the final inverting amplifier stage is roughly equal to U2A, and can be calculated as:

$$G_{U2B} = \frac{R13}{R12} \tag{33}$$

C3 and R12 together form a first-order highpass filter, and R11 is balancing R12 and R13 in order to compensate for the input bias current of the operational amplifier. The design characteristics for the final stage inverting amplifier is the same as for the final stage in the non-inverting signal path, with the exception of output polarity.

The compensation capacitors, C93 and C94 are again slightly larger than necessary in the 6.8 GHz and 10.65 GHz receivers in order to slightly decrease the slew rate of the operational amplifiers. This limits the high-frequency components of the noise signal and eliminates some of the effects from glitches in the noise signal caused by the Dicke switch.

4.1.5. The DC connected signal path

In a total power radiometer the LF amplifier measures the DC voltage from the RF detector diode, and must therefore be entirely DC connected. The LF amplifier designed for this thesis includes a DC connected signal path, which needs to be used when the LF amplifier is used in a total power radiometer. The DC connected signal path may also be manually enabled by the control processor for testing purposes.

The output signal from the RF detector diode in a radiometer receiver contains a fundamental DC offset voltage in addition to the noise signal. The offset voltage is different in each receiver channel, and is very difficult to estimate in advance. This makes designing a fixed DC offset compensation circuit impossible. For this reason, a tuning potentiometer was been added to correct for this in the DC connected signal path in the LF amplifier. The AC connected signal path does not have this problem, and does not need a tuning potentiometer.

The DC connected LF amplifier branch is implemented with operational amplifiers U3A and U3B. Both amplifiers are connected as non-inverting DC amplifiers, each with a first-order lowpass RC-filter at the input. In addition, U3A has a DC offset adjustment potentiometer, R21 connected to its feedback network.

Table 4.5. U3A and U3B amplifier component values

	6.8 GHz	**10.65 GHz**	**18.7 GHz**
R14	1 MΩ	1 MΩ	1 MΩ
R15	1 MΩ	1 MΩ	1 MΩ
R16	47.5 kΩ	51.1 kΩ	47.5 kΩ
R17	47.5 kΩ	47.5 kΩ	47.5 kΩ
R18	10 kΩ	10 kΩ	10 kΩ
R19	47.5 kΩ	20 kΩ	47.5 kΩ
R20	47.5 kΩ	20 kΩ	47.5 kΩ
R21	100 Ω	100 Ω	100 Ω
C4	1 µF	1 µF	1 µF
C5	1 µF	1 µF	1 µF
C6	22 µF	22 µF	22 µF
C95	33 pF	220 pF	22 pF
C96	33 pF	220 pF	22 pF

The RF detector diode typically produces a negative output voltage of a few millivolts, a voltage that would saturate the later amplifier stages in the DC connected signal paths unless compensated for. The offset voltage is different in every radiometer channel and may also vary over time, so a fixed offset voltage cannot be used. The offset adjustment range can be calculated from the voltage divider consisting of R18 and R21.

$$U_{max} = \frac{R21}{R18 + R21} VCC\_ \tag{34}$$

This gives a maximum offset voltage of -120 millivolts for all the receivers when powered by a negative a supply voltage of -12 volts. Reduced to the LF amplifier input, this

is -12 millivolts for the 10.65 GHz receiver and -24 millivolts for the other receivers. The DC offset adjustment voltage is filtered by a large bypass capacitor, C6.

The voltage gain of U3A and U3B can be calculated in the same way as for the other non-inverting amplifiers, and by substituting the correct components, we get

$$G_{U3A} = \frac{R14 + R20}{R20} \tag{35}$$

$$G_{U3B} = \frac{R15 + R17}{R17} \tag{36}$$

The voltage gain is 22 for the DC connected amplifier stages in all radiometers except for U3A in the 10.65 GHz receiver, where the voltage gain is tuned to 51.

The input offset current of the operational amplifier is corrected by balancing R19 and R20 at the inputs of U3A, and R16 and R17 at the inputs of U3B. U3A has a first-order lowpass filter consisting of R19 and C4, and U3B has a functionally equivalent filter consisting of R16 and C5. The response times of the lowpass filters in the DC connected amplifier stages can be calculated as

$$\tau_{U3A} = R19 \cdot C4 \tag{37}$$

$$\tau_{U3B} = R16 \cdot C5 \tag{38}$$

giving a time coefficient of 20 milliseconds for U3A in the 10.65 GHz receiver and approximately 50 ms for all the other DC-connected amplifiers. The different time coefficient in the 10.65 GHz receiver is due to the difference in the resistors in the feedback network for the operational amplifiers, and has not been compensated for by changing the corresponding capacitors. The time coefficient is considerably smaller than a typical integration time of 500 milliseconds, in order not to affect the data sampling of the radiometer.

4.1.6. LF amplifier design characteristics

The final characteristics of the LF amplifier are summarized in table 4.6. These characteristics are theoretical values, calculated from the component values used. Some of the amplifier parameters have been tuned experimentally several times while building the HUTRAD radiometer system. Especially the LF amplifier gain has been the subject of tuning during the building of the radiometer system, because the required gain was not known precisely in advance and experimental tuning was the only way to find suitable gain for each of the receivers. The 10.65 GHz proved particularly troublesome, because the RF components in this receiver deliver a much weaker signal to the LF amplifier than in the other receivers.

The frequency response and slew rate of the LF amplifiers have also been experimentally tuned using a digitising oscilloscope, and the correct function of the LF amplifier

and synchronous detector have been verified visually by observing the signal waveforms on the oscilloscope screen.

Table 4.6. LF amplifier design characteristics.

Design parameter	**6.8 GHz**	**10.65 GHz**	**18.7 GHz**
Gain (U1A)	13.5 dB	20 dB	13.5 dB
Gain (U1B)	27 dB	34 dB	27 dB
Highpass cutoff frequency	3.4 Hz	8 Hz	3.4 Hz
Gain (U2A)	27 dB	27 dB	27 dB
Highpass cutoff frequency	3.4 Hz	3.4 Hz	3.4 Hz
Gain (U2B)	26.5 dB	26 dB	26.5 dB
Highpass cutoff frequency	3.4 Hz	3.4 Hz	3.4 Hz
Offset adjustment range	-24 - 0 mV	-12 - 0 mV	-24 - 0 mV
Gain (U3A)	27 dB	34 dB	27 dB
Lowpass Filter time constant (U3A)	47.5 ms	20 ms	47.5 ms
Gain (U3B)	27 dB	27 dB	27 dB
Lowpass Filter time constant (U3B)	47.5 ms	51.1 ms	47.5 ms
Total gain (Non-inverting AC branch)	**67.5 dB**	**81 dB**	**67.5 dB**
Total gain (Inverting AC branch)	**67 dB**	**80 dB**	**67 dB**
Total gain (DC branch)	**67.5 dB**	**81 dB**	**67.5 dB**

Note that the gain of the two AC connected branches, U2A and U2B, are not exactly equal as they should theoretically be. Even so, this does not have a noticeable effect on the radiometer's performance as a whole, because the error caused by this gain imbalance is very small compared to the overall gain, and the error is also linear by nature. Any amplifier error that is linear, is fully cancelled out by the calibration procedure of the radiometer receiver chain.

The proper function of the LF amplifiers has been verified by measuring the waveforms with an oscilloscope in the synchronous detector, and by measuring the step response of the entire radiometer chain in the 6.8 GHz radiometer. The linearity of the entire radiometer receiver chain has also been tested for the same receiver, and the results can be assumed to apply equally to the other receivers. The measurement results are presented in chapter 5 of this thesis.

4.2. Synchronous detector and amplifier control

A Dicke radiometer needs a signal switch to alternate between the non-inverting and inverting signal paths in order to properly merge the signal after the LF amplifier. The switch should change position synchronously with the Dicke switch at the input of the radiometer receiver.

The LF amplifier designed for this thesis also has a separate DC connected signal path, and consequently has three separate LF signal paths. Only one of these may be connected to the output at a time, and some kind of control logic is needed in order to ensure this.

The synchronous detector is implemented with a standard CMOS 4066 quad bilateral switch integrated circuit and a few other peripheral components. The synchronous detector circuit itself is built on the same circuit board as the LF amplifier, together with the core of the amplifier control logic. Figure 4.2. shows the circuit diagram of the synchronous detector and amplifier control. Circuit board boundaries are marked with a dashed line in the diagram. The Dicke switch drivers needed for the 6.8 GHz and 10.65 GHz receivers are installed in separate enclosures, and are mechanically attached to the Dicke switches themselves.

The Dicke frequency and the mode control signal from the control processor are fed through optoisolators in order to avoid electrical interference entering through the cables. This also allows the control signals to be safely hot-plugged without turning off the power for the radiometer or the control computer. The Dicke frequency signal is also split to the Dicke switch drivers just after the optoisolator.

The amplitude of the input signal from the three signal paths is usually only a few volts, but can be as high as ±10 volts under extreme conditions, for instance if strong interference enters the radiometer receiver through the antenna. The V-to-F converter, on the other hand, can only handle a positive voltage in the range of 0-15 volts. The signal amplitude is limited to a voltage range of approximately -5 to +8 volts by a resistor and a 13 volt zener diode. The signal is also level-shifted up 5 volts by connecting the ground pin of the V-to-F converter circuit to the negative -5 volts supply. This results in an input voltage range of 0-13 volts at the V-to-F converter circuit input.

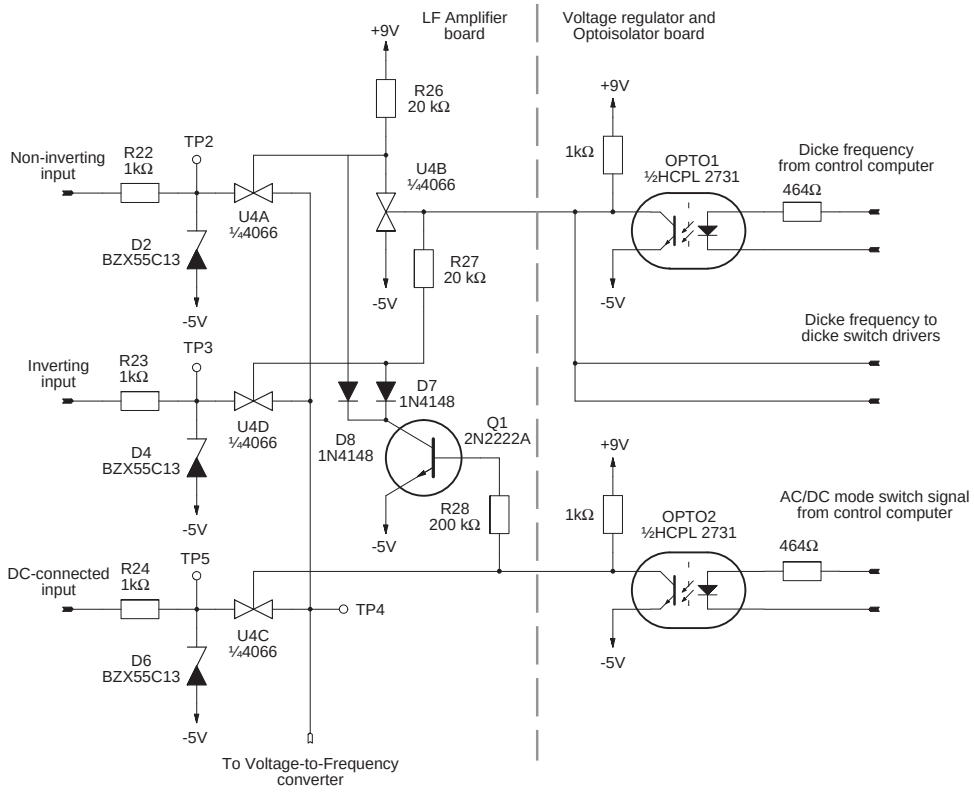

Figure 4.2. Synchronous detector and amplifier control circuit diagram.

The analog switches U4A and U4D in the two topmost signal branches together form the core of the synchronous detector. A third signal branch optionally feeds the

DC-connected signal via U4C. Only one of these signal paths may be active at a time, and this is guaranteed by the additional logic implemented with U4B, Q1, D7 and D8.

The Dicke switch control signal is used to select between either the inverting or the non-inverting signal paths. When a logic high signal level is applied to optoisolator OPTO1, its transistor will conduct and drive the voltage at its output collector towards -5 volts. This will effectively invert the control signal, which is then fed via resistor R27 to U4D, which will close the inverting input. The inverted signal is also fed to an additional analog CMOS switch U4B, which is connected as an inverter. The output from this inverter thus becomes effectively non-inverted with regard to the control signal from the control computer, and controls the analog switch U4A which in turn opens the signal path from the non-inverting input.

A logic low signal at the input of OPTO1 will reverse the functions described above, thus closing the non-inverting input and opening the CMOS switch U4A at the non-inverting signal input.

A logic high signal at the mode switch input, lights up the diode in optoisolator OPTO2, driving its collector voltage towards -5 volts. This will prevent Q1 and U4C from conducting, thus effectively keeping the DC-connected signal branch closed.

If a logical low signal is applied to the mode switch input, the CMOS analog switch U4C opens, allowing the DC-connected signal to be passed along to the Voltage-to--Frequency converter. At the same time, transistor Q1 will conduct, forcing the control voltage fed to CMOS switches U4A and U4D towards -5 volts via diodes D7 and D8. This will disable the AC-connected signal paths, while the DC-connected signal path is selected.

4.3. Voltage-to-frequency converter and integrator

The analog signal needs to be integrated and digitised before it can be handled by the control processor, and the integration time should be adjustable in order to suit the measurement requirements. The antenna footprint of the radiometer receiver varies according to altitude and flight speed, so adjustment should preferably be possible in flight.

The analog signal is integrated and digitised by a voltage-to-frequency converter circuit in the radiometer receiver and a 16-bit counter in the control processor unit; one for each radiometer channel. This is a simple arrangement allowing the data to be precisely integrated with minimal effort from the controlling computer. The schematic diagram of the Voltage-to-Frequency converter circuit is shown in figure 4.3.

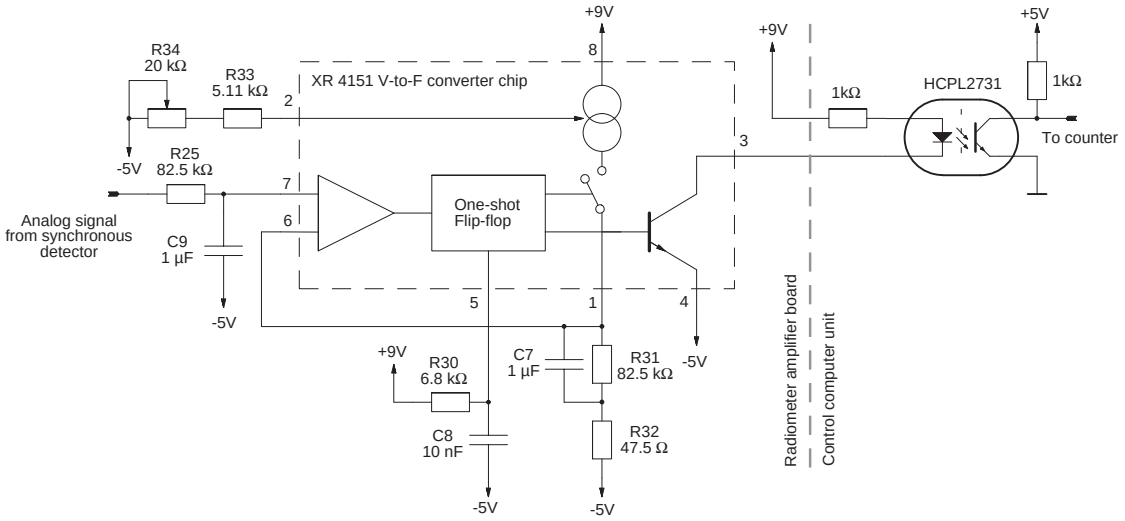

Figure 4.3. Analog data integrator circuit diagram.

The main component in the V-to-F converter and integrator circuit is a XR 4151 voltage-to-frequency converter chip from EXAR. [39] This is a pin-to-pin compatible low cost clone of the LM331 from National Semiconductor. [40]

In principle, the V-to-F converter consists of a short-time integrator and a single-shot flip-flop. The flip-flop triggers a single pulse every time a certain amount of current has flown into C9 at the input comparator, and this current integral will be completed faster at larger input voltages, thus outputting a higher frequency for a higher input voltage. The output frequency can be calculated as

$$f_{OUT} = 0.486 \cdot \frac{R33 + R34}{R31 \cdot R30 \cdot C8} \cdot V_{IN} \qquad (39)$$

The full-scale output frequency, and consequently the system gain, can be adjusted with potentiometer R34 and is typically set to approximately 10 kHz. The frequency varies according to the input voltage, and quickly follows a step in the input voltage, provided that C7 equals C9 and R25 equals R31. This keeps the step response of the radiometer good, and minimizes the effect from adjacent data samples on each other. The step response of the 6.8 GHz receiver has been measured, an the result is presented in the next chapter of this thesis.

The frequency produced by the V-to-F converter is still temporally continuous, but has discrete amplitude, and can thus be transmitted over some distance without risk of electrical interference. In the HUTRAD system, the different radiometer receivers transmit the signal a few meters to the controlling processor module, that handles data integration for several radiometers at a time.

The control processor has one 16-bit pulse counter for each radiometer channel and a separate integration time counter. The integration time counter drives the enable signal on each of the integration timers during the specified integration time. Counting stops immediately after the integration time has expired, and the control computer is signalled to read the contents of the integration timers and start the next integration cycle after that. There will consequently be a small amount of time between each of the integration periods, and a small percentage of the noise signal will be lost during this time. The

integration period isl not synchronized to any time reference, and cross-referencing the data to any other data requires interpolation of adjacent data samples.

4.4. Dicke switch drivers

The Dicke switch drivers are needed in the 6.8 and 10.65 GHz receivers, because the Dicke switches used in these two receivers require two control signals of opposite polarity. These Dicke switches are essentially two on/off switches put together, and need proper control logic in order to prevent impedance mismatches caused by both signal branches entering the same state simultaneously. This is accomplished with two comparators, one inverting and one non-inverting. The circuit diagram of the Dicke switch driver is shown in figure 4.4.

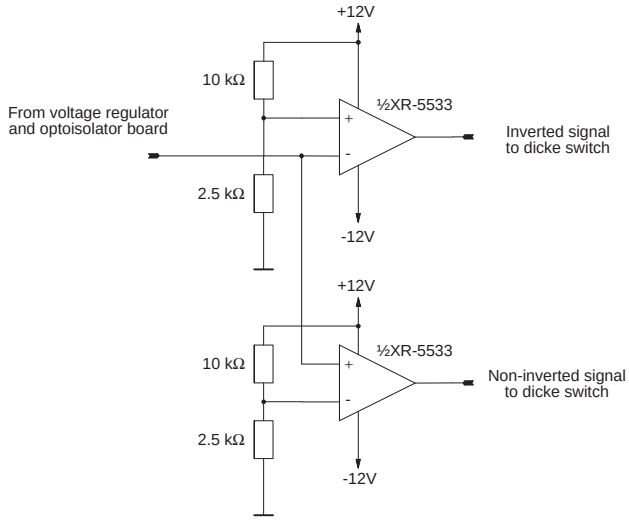

Figure 4.4. Dicke switch driver circuit diagram.

A dual operational amplifier of the same type as used in the LF amplifier has been connected as a comparator with +2.5 volts as the reference. One of the operational amplifiers has the input signal connected to the positive input and the reference connected to the negative input, while the other operational amplifier is connected the other way round. This effectively produces one non-inverted and one inverted output signal as needed by the Dicke switch. This circuit is only used in the 6.8 and 10.65 GHz radiometers, because the Dicke switch used in the 18.7 GHz receiver can be driven directly from the optoisolator on the voltage regulator and optoisolator circuit board.

4.5. Peltier element drivers

The temperature control in the radiometer receiver boxes is implemented with solid-state Peltier heat pumps. The Peltier elements are electrically symmetrical, and capable of both heating and cooling the radiometer receiver. The direction of the heat transfer is changed simply by reversing the direction of the current.

These Peltier elements are driven by power MOSFET bridges designed and built by Mr. Ilkka Mononen. These bridges are not part of the author's work for this thesis, but they are briefly described here because they are an essential part of the temperature control subsystem of HUTRAD. The circuit diagram of one of the Peltier element driver bridges is shown in figure 4.5.

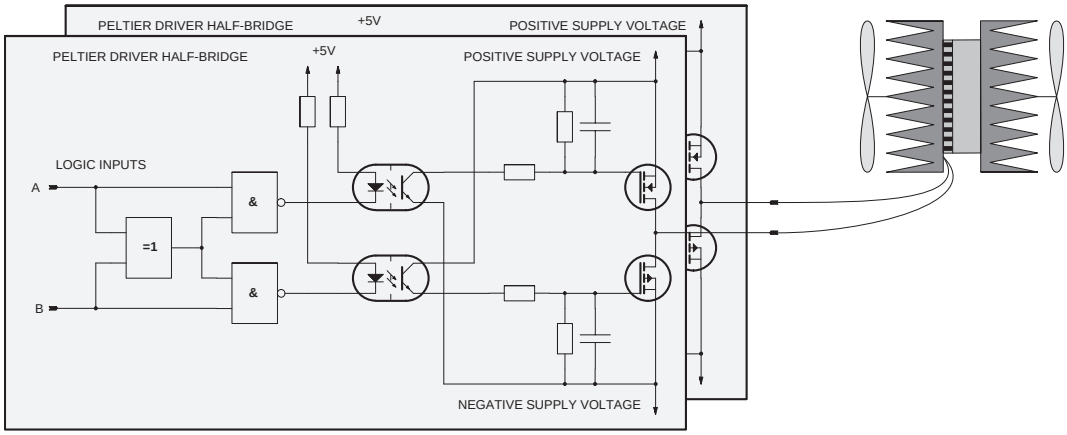

Figure 4.5. One of the Peltier element MOSFET driver bridges.

The output power can be regulated continuously by quickly switching on and off the MOSFET bridge with a variable duty cycle. Switching is implemented in software, and the switching subroutine runs in the background of the control processor with a frequency of a few cycles per second. The control software can run up to four PWM switching outputs in parallel, but the current HUTRAD system uses only three outputs per receiver unit.

The bridge is driven by a larger voltage than the control computer, and is connected to the control processor via optoisolators. The optoisolators protect the computer from possible faults and electrical interference from the driver bridge and vice versa.

The driver circuit also has a simple logic circuit that prevents the bridge from turning on in both directions at the same time, thus protecting the MOSFET bridge from short-circuiting itself even if the control software tries it. This protects the hardware from failing due to software bugs.

5. Measurement Results

5.1. Dicke switch driver test

The Dicke switches in the 6.8 GHz and 10.65 GHz receivers require two control signals of approximately ±10-12 volts with opposite polarities, and this control signal is output by a small amplifier circuit designed for this purpose. The input signal to the amplifier is a TTL-level signal fed through an optocoupler from the control processor module.

The output signal from the Dicke switch driver was measured with a digitising oscilloscope connected to a PC, and the measured data was analysed and plotted using a spreadsheet program. The control signals output to one of the Dicke switches is shown in figure 5.1.

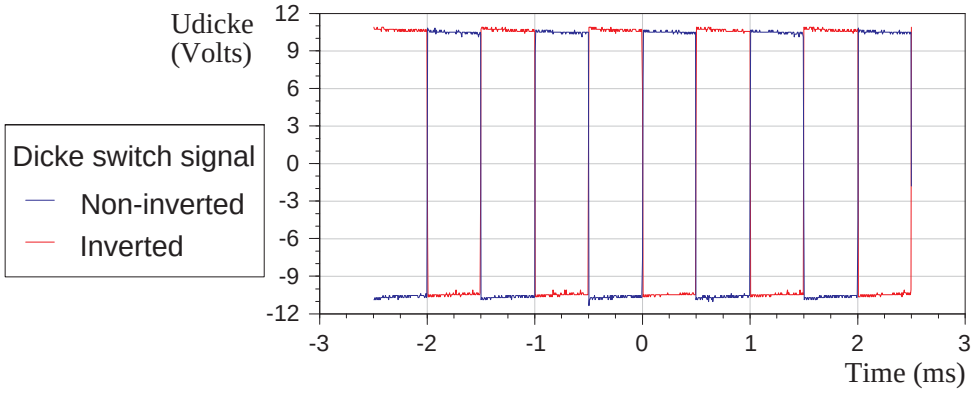

Figure 5.1. Dicke switch control signals

The Dicke frequency was programmed to 1 kHz by the control processor, and the signal's output from the driver to the two Dicke switch inputs is plotted with blue and red colours in the same graph.

As can be seen from the graph, the signal is a square-wave, with only fairly small errors visible in the graph. The zero-crossing occurs rapidly, and the voltage level is sufficient to drive the Dicke switches as required.

5.2. LF amplifier tests

5.2.1. Oscilloscope measurements during simulated cold calibration

Correct function of the LF circuitry was verified in the laboratory by simulating cold and hot load calibrations for the entire 6.8 GHz radiometer receiver. The signals that appear during cold calibration usually have the largest amplitude that will ever occur in the LF amplifier, and if the amplifier performs as designed during cold calibration and

warm calibration it can be assumed to perform well for all intermediate input signal levels.

Signal conditions equivalent to cold calibration were simulated by connecting 50Ω terminating resistors to the antenna inputs and submerging these terminating resistors in liquid nitrogen. The thermal noise power emitted by a terminating resistor submerged in liquid nitrogen is equivalent to a radiometer antenna brightness temperature of 77 kelvins. The signals present at the synchronous detector during the cold calibration simulation are shown in the figures 5.2 to 5.4.

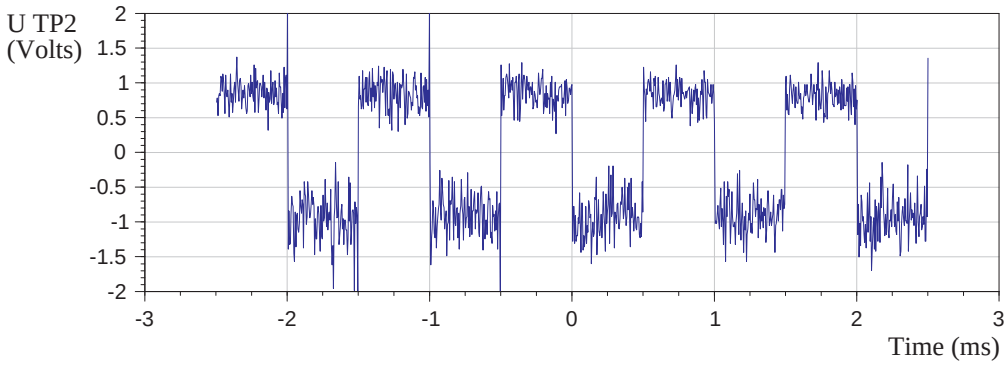

Figure 5.2. Non-inverted signal at TP2 during cold calibration

The cold calibration data clearly show the difference in noise signal strength between the cold calibration load and the Dicke reference. Because the LF amplifier is AC connected, the square wave signal will become centred at approximately zero. There is also a noise signal of approximately 0.3-0.4 volts RMS added to the square wave, but this noise will be effectively eliminated by the RC-filter at the Voltage-to-Frequency converter input. The integration time will also have an effect on the amount of noise remaining after integration, and basically longer integration times will reduce the amount of noise in the final radiometer data.

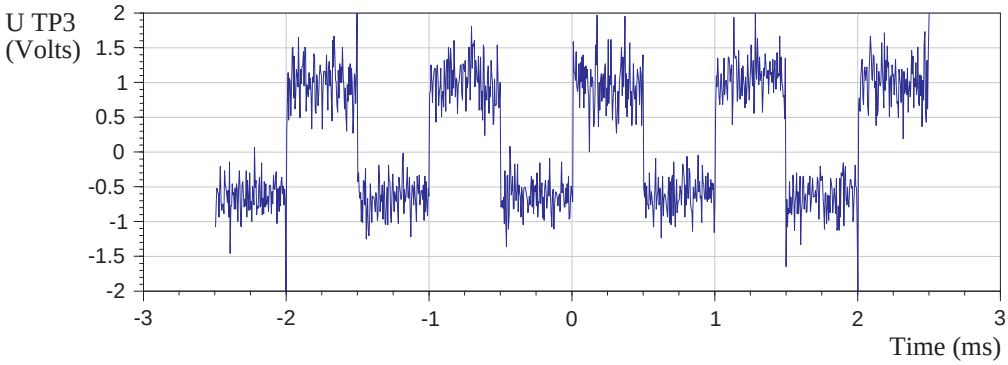

Figure 5.3. Inverted signal at TP3 during cold calibration

The inverted signal is basically the same as the non-inverted signal, but the square wave is phase shifted by 180 degrees. The phase shift has been verified by triggering the oscilloscope with the Dicke switch control signal. The operational amplifier in the

inverted signal path has an offset error of approximately +0.2 volts, which can be clearly seen in figure 5.3. The offset error is so small that it poses no risk for signal clipping in the amplifier, and will be fully eliminated by the radiometer calibration procedure.

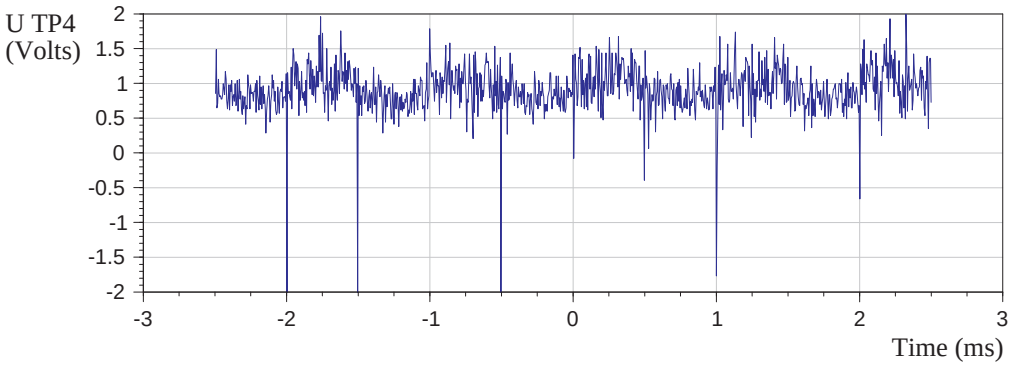

Figure 5.4. Combined signal at TP4 during cold calibration

The output from the synchronous detector is shown in figure 5.4. and the graph shows that the CMOS switch has selected the positive half-periods of the square wave signals present at the non-inverting and inverting signal paths. The offset error in the inverting signal path can be seen as a slightly smaller signal amplitude in the parts of the signal where the inverting signal has been selected. There are also a few glitches present in the signal at the switching point of the CMOS switch, but the glitches are very short and thus their contribution to the radiometer output is small. The average signal level, which is output to the V-to-F converter is approximately 0.9 volts.

As can be clearly seen, the LF amplifier and synchronous detector works as designed, although a slight offset error is visible in the output of the inverting signal path. Note also, that an input brightness temperature colder than the reference temperature at the Dicke switch produces a positive output voltage, which gives a negative-signed gain for the entire radiometer chain.

5.2.2. Oscilloscope measurements during simulated warm calibration

Warm calibration was simulated at room temperature by connecting 50Ω terminating resistors to the antenna inputs of the same receiver as during the cold calibration simulation. This produced a minimal difference in brightness temperature between the input signal and the Dicke reference signal, and represents the input signal with the smallest possible amplitude that can be present at the synchronous detector. The same three test points at the synchronous detector that were used in the cold calibration test were used in this test also.

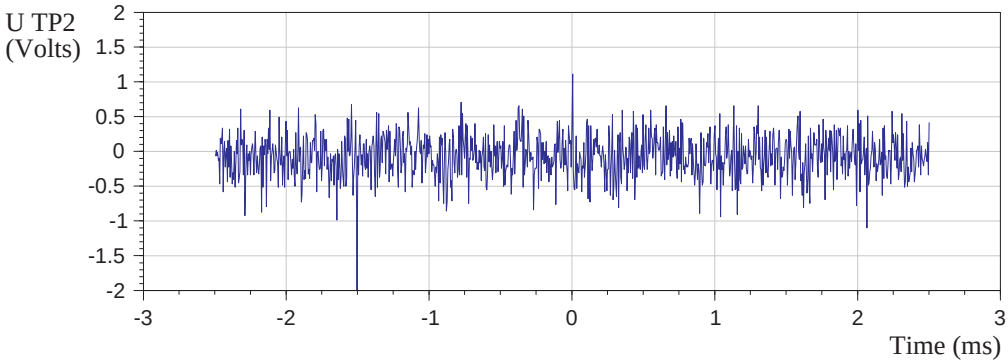

Figure 5.5. Non-inverted signal at TP2 during warm calibration

The square wave from the Dicke switch is now almost completely absent, because the reference temperature is very close to the brightness temperature at the antenna input. The remaining signal is white noise with an amplitude of approximately 0.3 volts RMS, as was the case during the cold calibration test.

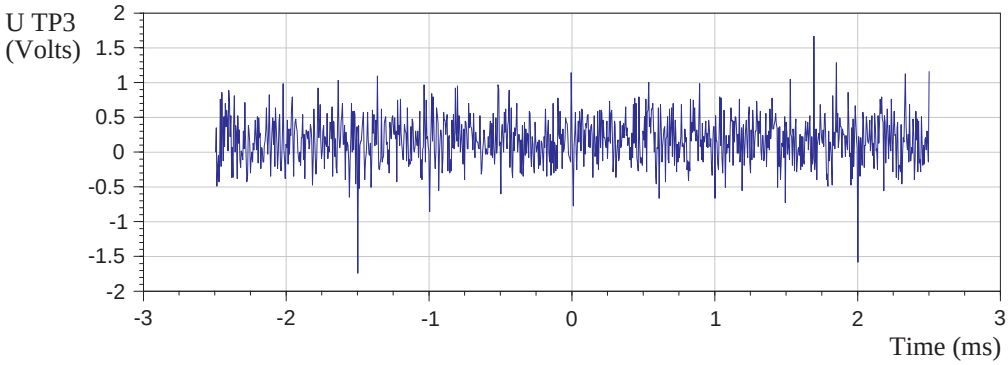

Figure 5.6. Inverted signal at TP3 during warm calibration

The inverting signal path shows roughly the same offset error of +0.2 volts that also was present in the cold calibration test. Otherwise the inverting signal path performs completely as designed.

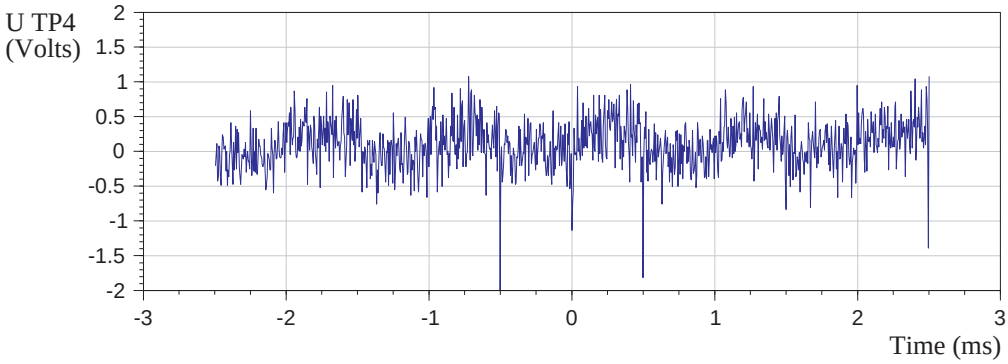

Figure 5.7. Combined signal at TP4 during warm calibration

The output after the synchronous detector shows a square wave with a small amplitude, because the two signal paths with different offset errors have been combined here. The resulting offset error is the mean value of the offset errors of the non-inverting and inverting signal paths. In practice, this means that the dominant offset error, which is in the inverting signal path is halved in the output signal.

The DC component of the offset error is eliminated by calibrating the radiometer, and any effect of this signal component can be fully eliminated, if the integration time is an integral multiple of the period of the Dicke frequency. This condition should be fulfilled anyway, because otherwise aliased components of the Dicke frequency will be visible in the data at all brightness temperatures that differ from the Dicke reference temperature.

5.3. Laboratory tests of the radiometer

5.3.1. Radiometer step response

The step response was measured for the horizontal polarisation channel of the 10.65 GHz receiver. A step in the brightness temperature was simulated using an electrically operated two-way RF switch at one of the antenna inputs. One of the RF switch inputs was connected to a terminating resistor at room temperature and the other input of the RF switch was connected to a terminating resistor sumberged in liquid nitrogen. This setup introduces similar noise levels to the radiometer as when the radiometer is calibrated.

In order to minimize the response time of the radiometer, the integration time was set to the shortest possible value of 50 milliseconds. The radiometer data file was first analysed using Matlab, and the relevant data samples were extracted from the raw radiometer data. The data was then plotted with a spreadsheet program, and several of the noise power level transitions were merged on the same graph in order to visually compare the transitions to each other. The raw data from the step response test is plotted in figure 5.8. Note that the raw data value for a cold calibration target is higher than the raw data for a warm calibration target, because the gain of the entire radiometer chain has negative sign.

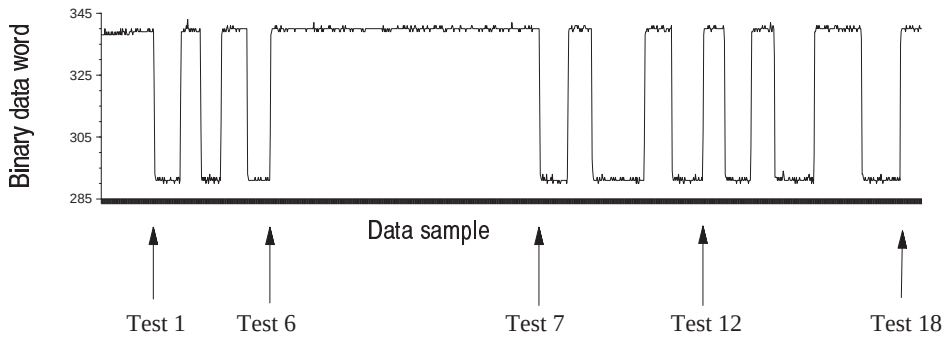

Figure 5.8. Plot of the raw data from the step response test

A step in the brightness temperature was introduced by flipping a mechanical switch a total of 18 times. The exact time when the switch was flipped was not in any way synchronised with the data integration timer, and consequently, there will be data samples that are somewhere in between the high and low values of the data samples in the graph. The response time is also limited by the integration time, and it is not possible to detect faster response times than twice the minimum integration time of 50 ms from the data. A zoomed plot of the three first step response tests for a transition from the cold calibration target to the hot calibration target is shown in figure 5.9.

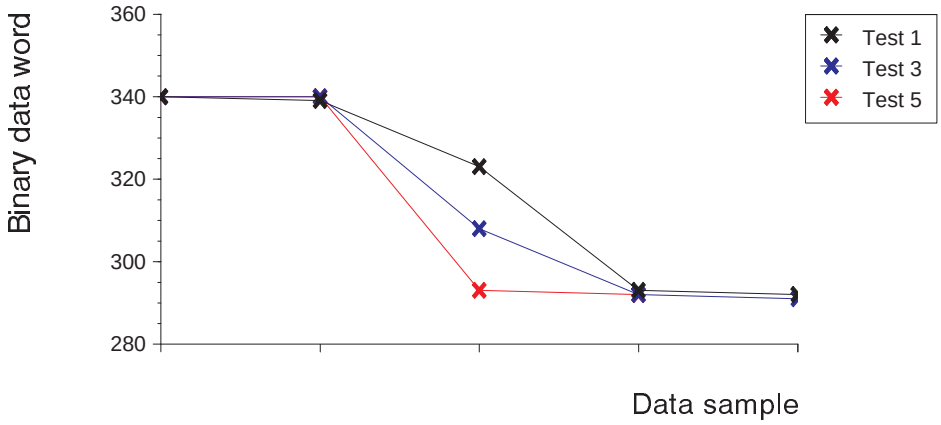

Figure 5.9. Detail of the three first cold-to-hot step response tests

The signal transitions have been horizontally aligned so that they can be compared to each other. As can be seen from the graph, there is a random timing variation between the different tests within two consecutive integration cycles. Test 1 and Test 3 show a data sample in the centre, where the switch has been flipped in the middle of an integration cycle. The corresponding data sample is somewhere in between the noise power levels corresponding to cold and hot calibration. Test 5 has happened to coincide well between two adjacent integration cycles, and show the sharpest possible signal transition of exactly 50 milliseconds.

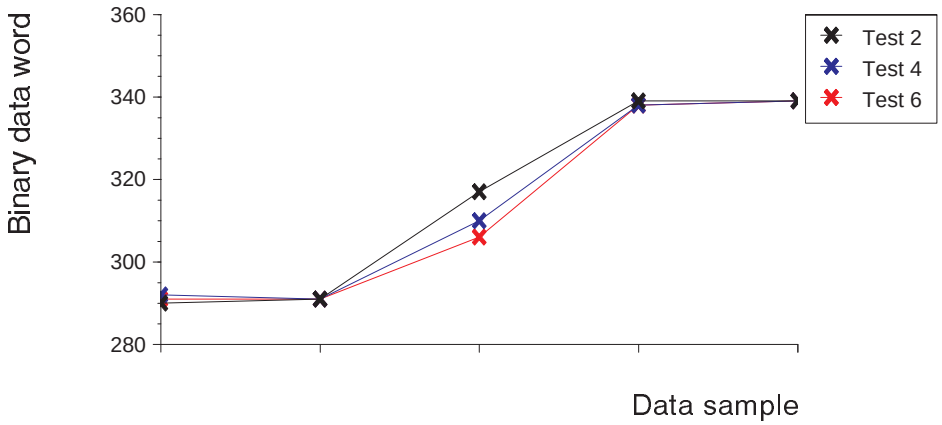

Figure 5.10. Detail of the three first hot-to-cold step response tests

The first three hot-to-cold signal transitions all happen to be roughly in the middle of an integration cycle. The step response test was repeated several times, and the remaining test results are plotted in figure 5.11.

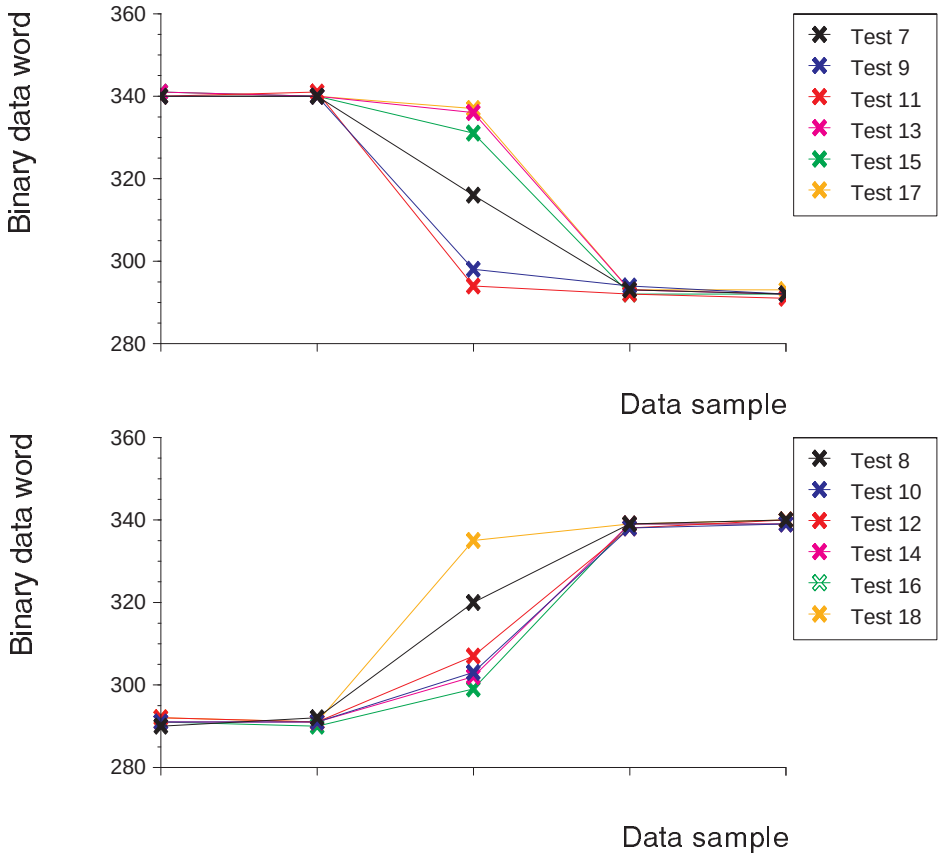

Figure 5.11. Step response test repetitions 7-18

These graphs show that the limiting factor for the step response is the integration time, and that the step response of the RF components and the LF amplifier is faster that the shortest possible integration time. The step response is important, because a poor step

response would result in blurring of adjacent data pixels in the measured data. A wise precaution that would even further reduce pixel blurring is to use a shorter integration time than theoretically is necessary, and then digitally resample the measured data to the desired resolution when analysing the data. Resampling the data also allows for the alignment of the radiometer data samples with data samples from other instruments.

5.3.2. Radiometer response linearity test

The linearity of the LF circuitry has not been tested by itself, but the linearity of the entire receiver chain in the LF radiometer units have been tested by Juha Lemmetyinen, and the measurement method and results are documented in his master's thesis. [1] The linearity test is not part of the author's work for this thesis, but the result is presented here as evidence of the linearity of the LF amplifier designed by the author.

Different brightness temperatures were simulated using a terminating resistor cooled with liquid nitrogen and a variable attenuator. An attenuation of 0 dB corresponds to a brightness temperature of 77 Kelvins, and increasing the attenuation increases the brightness temperature measured by the radiometer towards room temperature. The result of the linearity test for the horizontal channel of the 6.8 GHz receiver is plotted in figure 5.12.

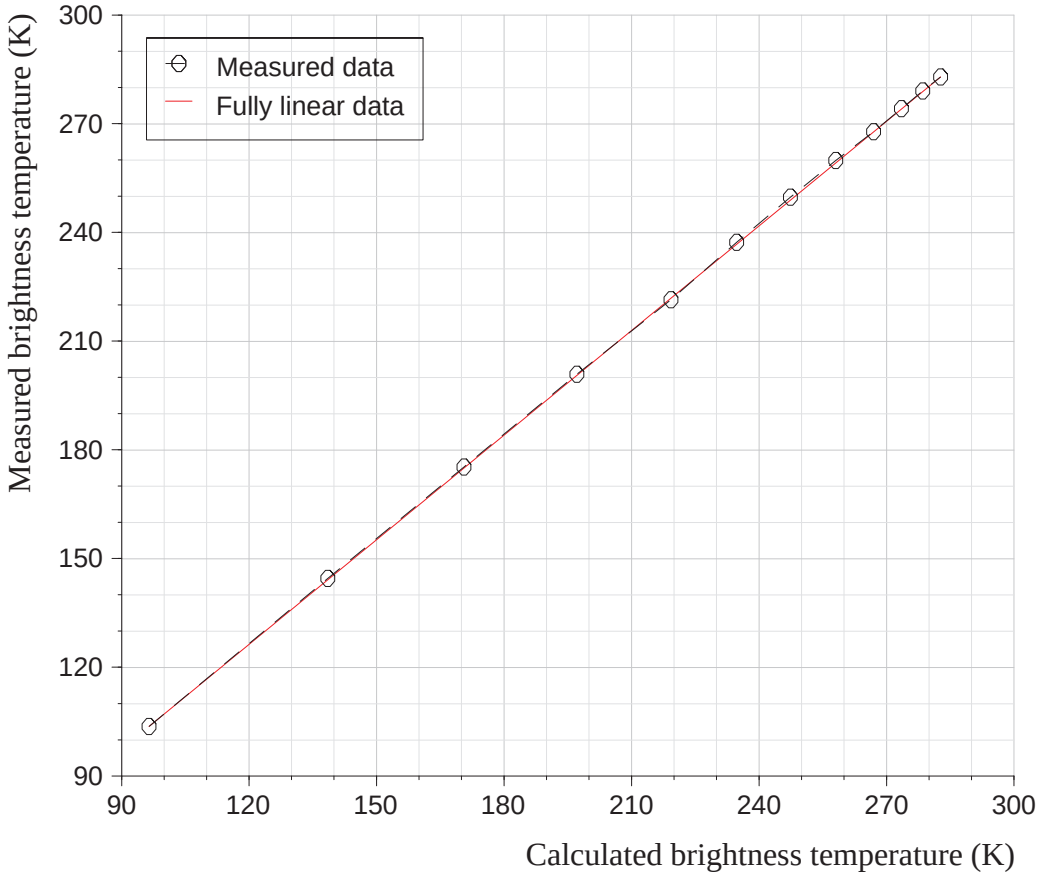

Figure 5.12. Calculated and measured brightness temperature.

The receiver was first calibrated normally using cold and hot reference targets. Several settings of the variable attenuator were measured with a VNA (Vector Network Analyser) and the corresponding theoretical brightness temperatures for the liquid nitrogen cooled terminator seen through the attenuator were calculated. The same attenuator settings were measured with the radiometer and the results were compared to each other.

The measurement error was larger at low brightness temperatures, because lower attenuation values are more difficult to measure precisely with the VNA. Connector and cable attenuation and mismatches also become more prominent at lower attenuation values, and an attenuation error of 0.1 dB might affect the resulting brightness temperature as much as 10 Kelvins. The measurement result here shows an error of approximately 7 Kelvins for the lowest attenuation value.

The linearity error of the entire radiometer receiver chain has been estimated by drawing a straight line between the two measurements at each end of the graph. In this case, the largest error was approximately 0.76 Kelvins at a brightness temperature of 249 Kelvins. If the reference points are excluded, the average error is only 0.36 Kelvins which can be considered quite good. Since the entire receiver is very linear, the LF circuitry can also be assumed to be linear.

5.3.3. Data transmission network test

The network performance was tested in the laboratory using an isolated measurement network in order to eliminate the effect of other network traffic on the test. The newer HF radiometer unit was operated in the same network in order to simulate typical network traffic present on the skyvan on a normal measurement flight. The integration time was set to the shortest possible value of 50 milliseconds in order to get as many data samples as possible in a reasonable time.

Table 5.1. Network data loss ratio test results

First packet of data	2
Missing packets	244845-244854
Last packet of data	250449
Successfully transmitted packets	250448
Lost packets	10
Packet loss ratio	0.004%

As can be seen from the results, some data packets have indeed been lost during this test, but the packet loss ratio is so small that it is insignificant compared to the total data volume. It is interesting to note that all ten packets lost are consecutive packets, indicating that the loss is caused by a single temporary disconnection in the network. At an integration time of 50 milliseconds, this disturbance in the network can be estimated to have been only half a second in duration.

Using a more sophisticated networking protocol with a proper handshaking algorithm would correct most of these temporary network problems. However, the probability of data loss is so small that the additional computing overhead is not likely to be worth the

effort. The current implementation of just blindly sending the data packets over the network works well enough by a large margin.

5.3.4. Data integrator timing accuracy test

The timing accuracy of the data integrator was measured at the same time as the network performance was tested. The time reference was taken from the NTP server at the TKK campus network, which in turn is synchronized to the centre for metrology and accreditation. The test results are summarized in table 5.2.

Table 5.2. Data integrator timing test results

	Sample number	Time stamp	Actual time
Beginning of data	2	700879	10:41:36.072
End of data	250449	943669	14:23:51.414
Time difference		242790	3:42:15.342
Integration cycles	250448		3:28:42.400
Missed integration time			0:13:32.942

The time stamp is expressed in MS-DOS timer ticks since midnight local time. The MS-DOS clock runs at a frequency of 18.2065 Hz, which gives a clock period of approximately 54.9 ms. The data integrator gate uses a programmable timer which can be set to an integral number of milliseconds. The counter runs independently of the MS-DOS clock, thus avoiding rounding problems when calculating the integration time value.

The data integrator counters are stopped for a small amount of time between each integration period, and the control processor must quickly read the result from all the data integrator counters before the next integration cycle can be started. The timing test took a total of 13335.34 seconds to complete 250448 integration cycles. The integrator gate counter was programmed to an integration time of 50 milliseconds, resulting in a total integration time of 12522.4 seconds. This leaves 812.94 seconds as the time when the integrator was not running during the test. Consequently, the "dead time" of the data integrator counters are approximately 3.25 ms per integration cycle. At a typical integration time of 500 ms, this will result in an integration time loss of approximately 0.65%.

5.3.5. Clock synchronisation test

The clock synchronisation was also tested simultaneously with the network performance. Coarse synchronization of the control processor clock was performed at start-up by the Novell Netware client installed in the control processor. The coarse clock synchronisation was only capable of synchronising the processor clock with a precision of ±1 second, and more precise synchronisation was maintained by the measurement software itself.

The software measures time in MS-DOS timer ticks, and engages whenever a clock offset of three ticks or more is detected. This limits the maximum clock offset for the

control processor module to 164.7 ms, when fully synchronised to the data storage server. The measurement software checks the time difference between the data storage server and the control processor module clock once per minute, and the control processor module adjusts its clock a maximum of two ticks at a time. This implies that if the processor module clock drift would be larger than 0.182%, synchronisation of the control processor would become impossible. The clock synchronisation events were read from the system log file, and the synchronisation events are plotted graphically in figure 5.13.

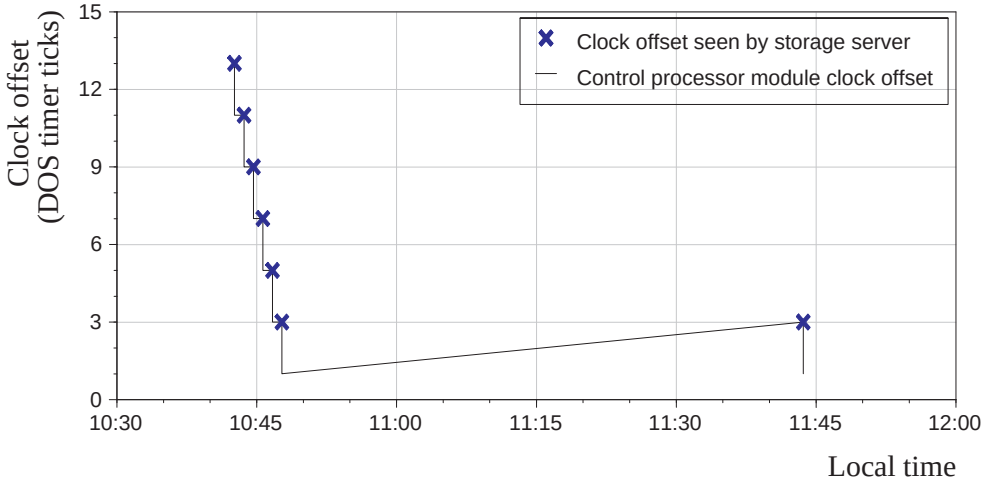

Figure 5.13. Radiometer unit clock offset and drift

At start-up, the software detected a clock offset of 13 ticks, and started to gradually adjust the control processor clock in six consecutive steps. The last of these step adjustments occurred at 10:47:42, and left a residual clock offset of a single MS-DOS timer tick. After this, the control processor clock offset remained within a limit of ±3 timer ticks until 11:43:37. If the clock drift of the control processor is assumed to be constant, the time error of the control processor can be interpolated by straight lines between the time synchronisation events. In this test, the drift of the control processor did not exceed 109.8 milliseconds in 3355 seconds, or 32.7 ppm. This can be considered to be normal clock drift for a quartz crystal based PC clock.

5.4. Field measurements

5.4.1. Receiver temperatures during warm up

Some of the receiver components are very sensitive to temperature variations and therefore, a stable temperature must be maintained inside the receiver enclosures during the entire calibration and measurement time. The radiometer system must be allowed to reach and stabilise the inside temperatures of the receivers for at least an estimated two hours, before the radiometers can be reliably operated.

Each receiver is equipped with four temperature sensors placed at different points inside the receiver. One of these sensors is selected as the controlling sensor, and the regulator

tries to keep the temperature of the controlling sensor as close as possible to the set temperature. The other temperature sensors will give a rough estimate of the temperature gradients present inside the receiver enclosure.

The HUTRAD radiometer system has been successfully operated many times during the years, and figures 5.14. to 5.16. show the receiver inside temperatures during the warm up period from a measurement campaign conducted on the 12th of May 2006. The inside temperature setting was +20 °C, and the controlling temperature sensor measured the air inside the receiver enclosures in all three receivers during this campaign.

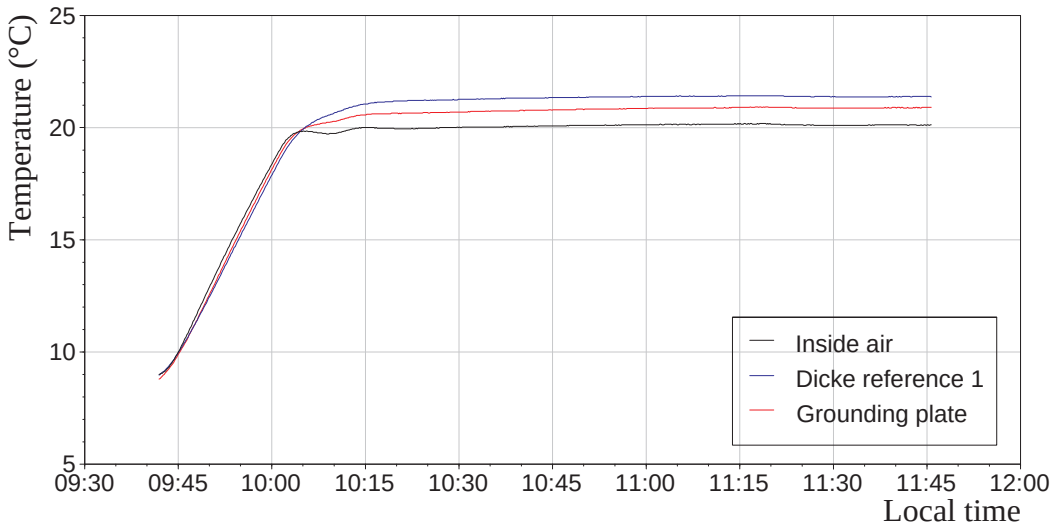

Figure 5.14. Warm up period of the 10.65 GHz receiver

The temperature control of the 10.65 GHz receiver works quite well, and this receiver can be considered ready for measurement after about one hour of warm up time. One of the temperature sensors was broken during this campaign, so only three graphs have been plotted here.

The temperature gradients present inside the receiver can be clearly seen and the heat generated by the components inside the receiver tend to raise the temperatures of the individual components slightly above the set temperature. The Dicke switch references are the warmest components measured in this receiver, because they are affected by the Dicke switch driver amplifiers. The temperature gradient is, however, not a problem as long as it is constant during calibration and measurement.

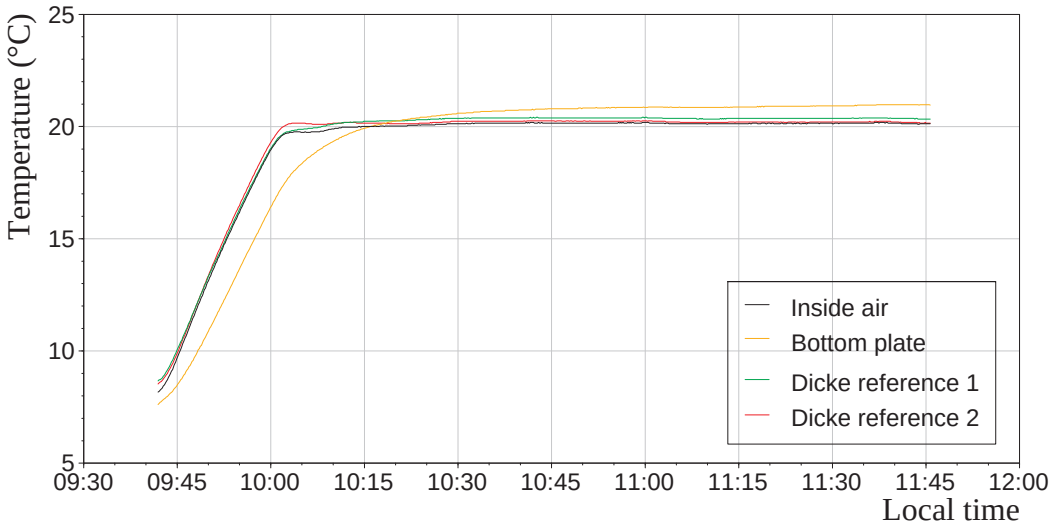

Figure 5.15. Warm up period of the 18.7 GHz receiver

The 18.7 GHz receiver has some bulky components mounted tightly on the bottom plate, and these components take more time to warm up. This receiver also stabilizes its temperature quite well within one hour after power on, but the components attached to the bottom plane reach a stable working temperature after one and a half hours. This is still well inside the estimated warm up time of two hours.

The temperature gradients inside this receiver are smaller than in the other receivers, because the components are mechanically mounted more tightly together. Also note, that the temperature of the Dicke switch references are closer to the set temperature because the Dicke switches used in this receiver do not need the additional Dicke switch driver and generate less heat than the Dicke switches in the other receivers.

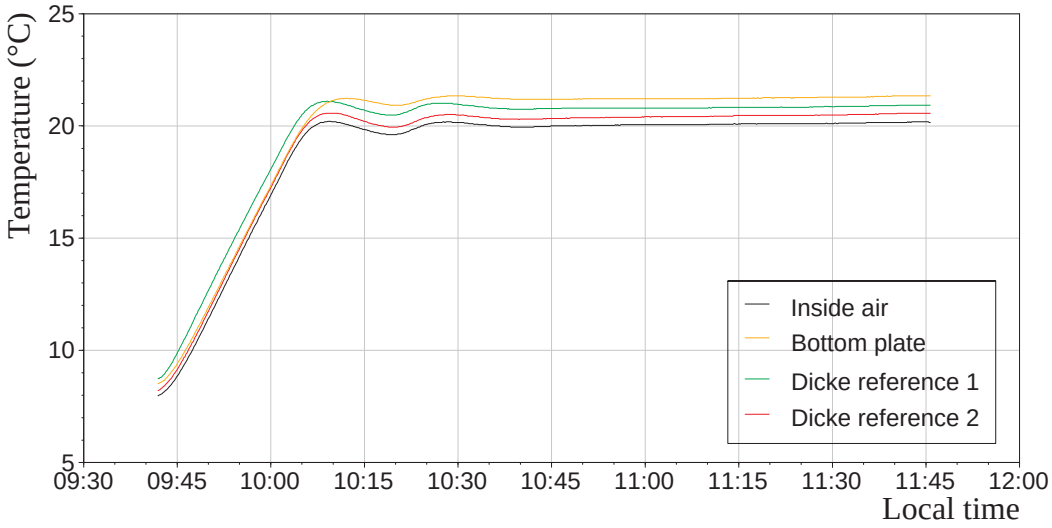

Figure 5.16. Warm up period of the 6.8 GHz receiver

The 6.8 GHz receiver behaves roughly in the same way as the 10.65 GHz receiver, but the tuning of the regulator loop is not as good. The regulator loop shows a slight

overshoot at the point where the set temperature is first reached and the temperature also oscillates a couple of times before the temperature stabilises. This receiver would benefit from some more tuning of the regulator parameters, even though the temperature eventually stabilises after approximately one hour.

After two hours, the inside temperatures of the 6.8 GHz receiver have increased slightly, because the ambient temperature has increased to almost the set temperature during the day of the measurement campaign. The Peltier heat pump has limited cooling capability, and the slight increase in receiver temperature indicates that the cooling effect has reached maximum power at this time. The 6.8 GHz receiver is also mechanically mounted just above the control processor, and the heat leakage from the control processor module has the greatest effect on this receiver. Figure 5.7. shows the ambient temperatures during this period.

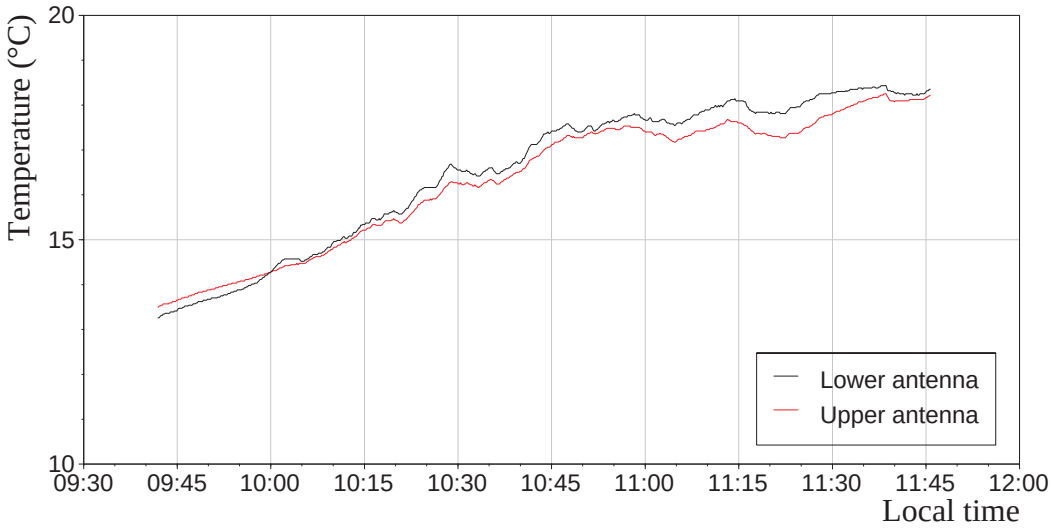

Figure 5.17. Antenna temperatures during warm-up period

The radiometer unit is equipped with two additional temperature sensors mounted in the antenna feed horns in the lower 6.8 GHz and upper 10.65 GHz antennae. These temperature sensors indicate the ambient temperature, and they here show how the outside temperature increased during the morning on 12th May 2006.

5.4.2. Temperature stabilising results

After the receiver temperature has been stabilised, the receivers may be calibrated and operated. The temperature regulators continue to keep the inside temperature of the receivers as constant as possible during the entire measurement campaign, and the most demanding part for the regulators is the actual measurement flight.

The ambient temperature can vary more than 10 degrees between ground level and measurement flight altitude, and the regulators need to keep the inside temperature as constant as possible during the entire flight. Figures 5.18 to 5.20. show the inside temperatures of the receivers during the flight of the measurement campaign conducted on the 12th of May 2006.

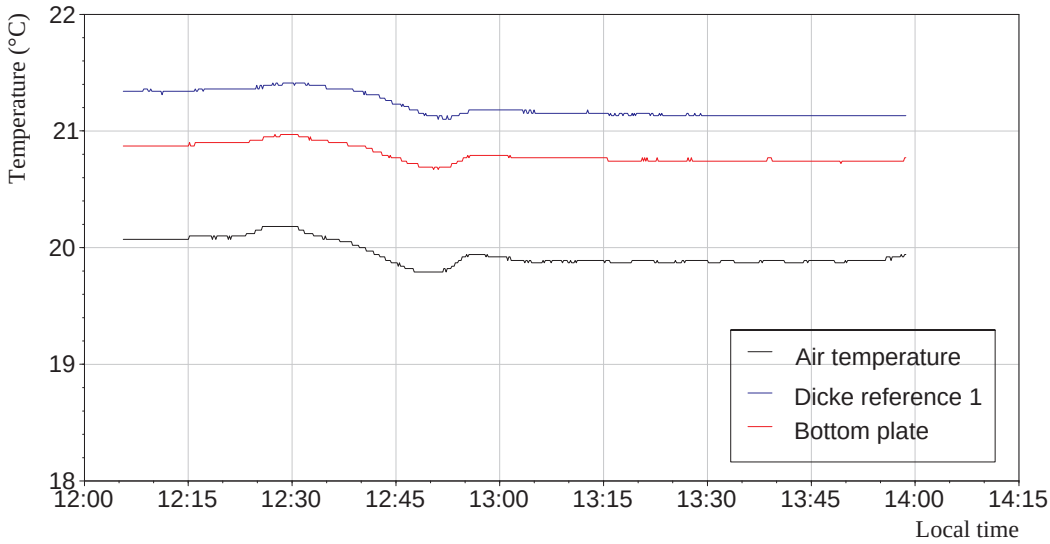

Figure 5.18. In-flight temperatures inside the 10.65 GHz receiver

The aircraft started to taxi along the runway at a approximately 12:20, and the hot exhaust gases from the engines caused the receiver temperature to rise slightly above the set temperature. Take-off was at approximately 12:35 and measurement altitude was reached at 12:45. The decrease in ambient temperature is visible as a slight undershoot just after measurement altitude has been reached. After this, the temperature was very stable until the end of the flight.

The temperature gradient between the air inside the receiver and the Dicke switch references decreased from approximately 1.3 degrees to 1.2 degrees, which indicates that the temperature gradient was not greatly affected by the outside temperature.

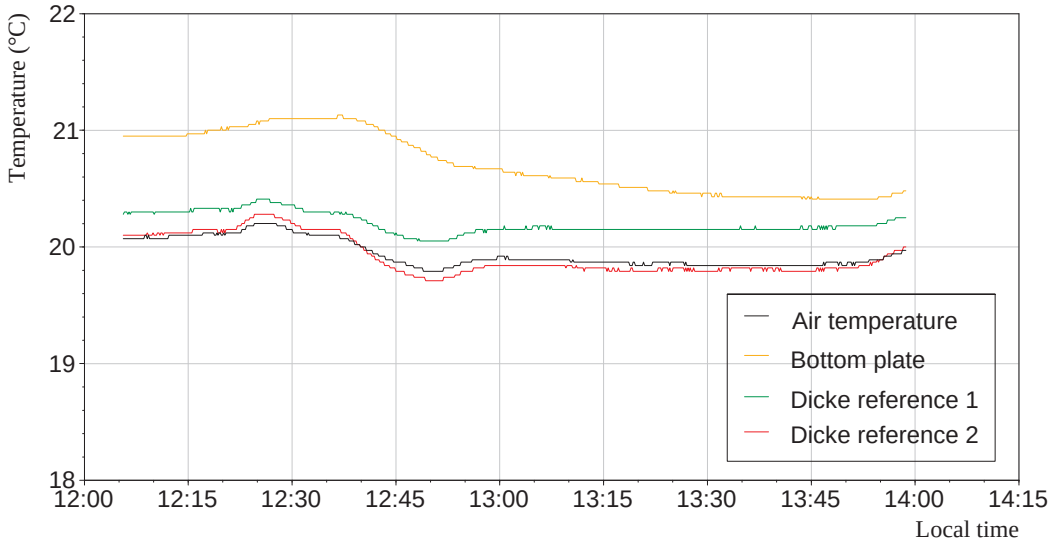

Figure 5.19. In-flight temperatures inside the 18.7 GHz receiver

The 18.7 GHz receiver has more trouble keeping the inside temperature constant because of the bulkier components. The antenna inputs of this receiver is connected via

waveguides, which cause heat to leak out from the receiver to the antenna inputs. The temperature gradient inside this receiver is also affected by this heat leakage, and a steady trend is visible in the graph throughout the measurement flight.

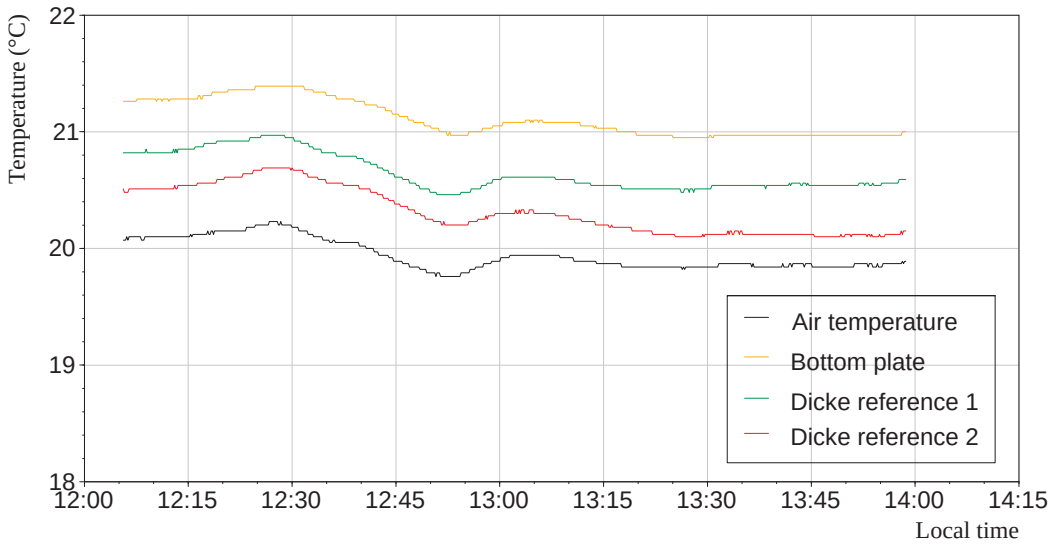

Figure 5.20. In-flight temperatures inside the 6.8 GHz receiver

The 6.8 GHz receiver also show a slight change in the inside temperature gradients, but not nearly as much as in the 18.7 GHz receiver. The two Dicke switch reference sensors show different temperature gradients during the measurement, and this is due to the fact that one of the Dicke switches is mounted closer to the rear side of the enclosure and heat leakage via the antenna cable is larger from this Dicke switch.

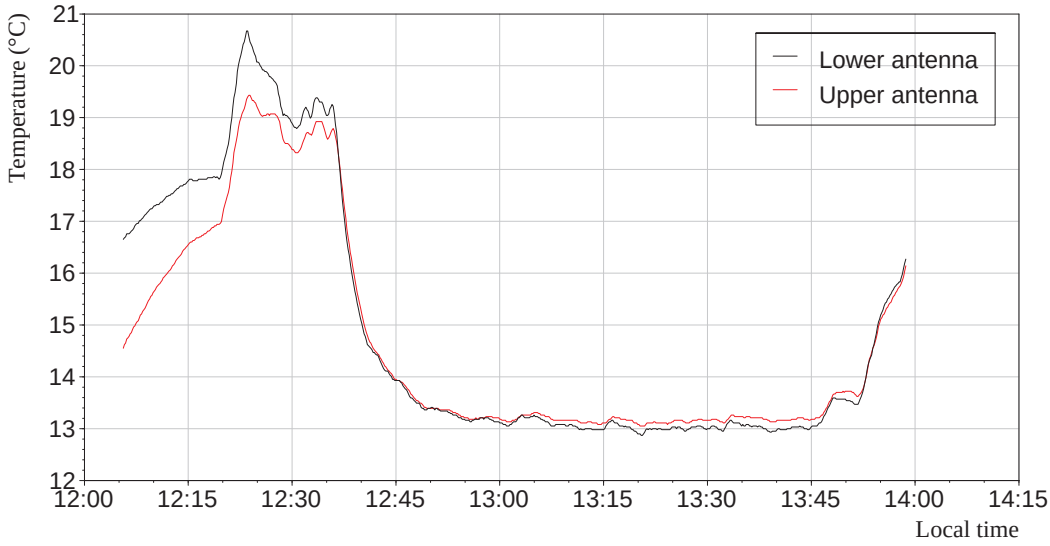

Figure 5.21. In-flight antenna temperatures

Figure 5.21. shows the antenna temperatures on the same measurement flight, and as can be seen, the ambient temperature varies heavily during the flight. The temperature rises a few degrees when the aircraft engines are started, and can vary further according

to wind direction and aircraft heading when the aircraft is on the runway. After takeoff the ambient temperature stabilises fairly quickly, and on this particular flight, the temperature at measurement altitude was approximately 13 degrees for the duration of the flight.

The temperature measurements show, that the temperature control works fairly well, but some improvements can still be done. The recommended warm up time for the radiometer system is two hours, but the temperature is fairly well stabilised already after just one hour. The set temperature should preferably be at least five degrees higher than the expected ambient temperature, but should not be set unnecessarily high because of the additional power consumption and prolonged warm up time.

5.5. Brightness temperature measurement

The HUTRAD radiometer system has been used in several remote sensing campaigns, and figure 5.22. shows a map [2] with the position of the aircraft marked on one test site from a campaign flown on the 18th of march 2005.

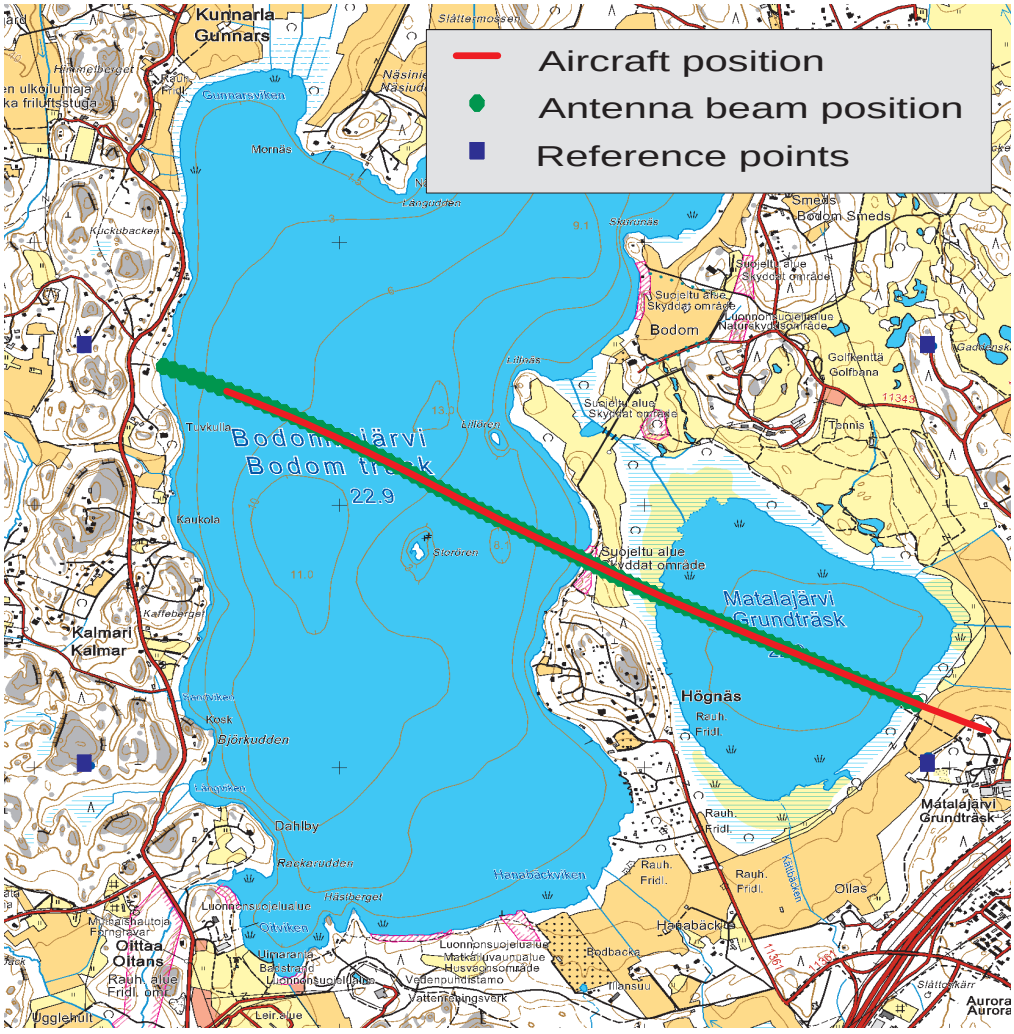

Figure 5.22. GPS position of the aircraft. Map Copyright © Maanmittauslaitos

Because the radiometer antennae look backwards from the aircraft at an incidence angle of approximately 50 degrees, the antenna footprint will be displaced from the aircraft position by a distance corresponding to the flight altitude. The correct position of the antenna footprint can be accurately calculated with the attitude data from the on-board inertial navigation system of the aircraft.

The GPS data recorded on the aircraft is marked in the figure with a thin red line, and the corresponding antenna footprint position is marked with a thicker green line. The aircraft crossed lake Bodom in a southeasterly direction, and consequently, the antenna footprint was a few hundred meters to the northwest of the aircraft position. The blue marks were used to align the GPS data with the digital map image. The corresponding brightness temperatures are plotted in figure 5.23. as a function of position along the flight track.

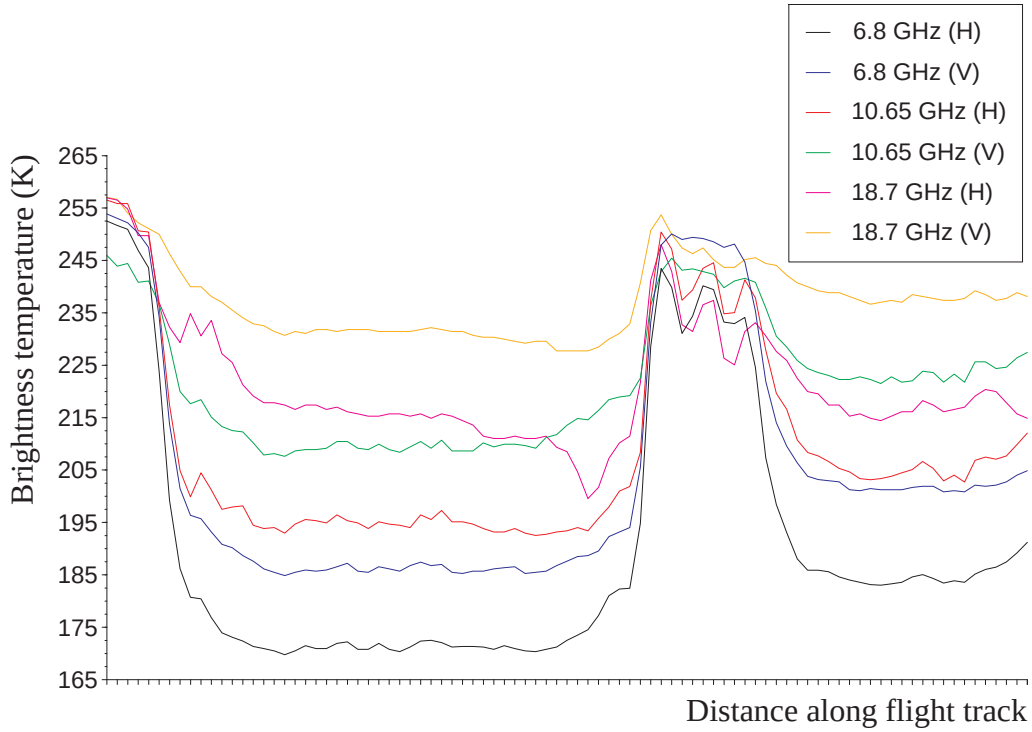

Figure 5.23. Brightness temperatures at lake Bodom

The brightness temperature drops rapidly, when the antenna beam hit the wet surface of the ice on the lake, and rose again when the narrow area of land was measured. The difference in brightness temperature is larger at the lower frequency, particularly in the vertical polarised channel. This is consistent with other observations.

6. Conclusions

6.1. The radiometer network

The radiometer network performs as expected, and the tests show that even though a transport protocol is not used, packet loss remains negligible for an isolated network. Time synchronization is also achieved with sufficient precision, and geolocation of the data is possible with a resolution well corresponding to the antenna beam footprint.

The asynchronous data sampling in the two radiometer units and the GPS receivers make data fusion slightly more laborious, but not in any way excessively. Sufficient geolocation precision can be achieved by linear interpolation of adjacent samples from the GPS data.

6.2. Software errors

There have been a few incidents with software bugs, some of which are still not properly corrected. The monitoring software had some timing issues, which caused the real time brightness temperature display to not be able to keep up with the data rate of the radiometer system. This caused problems when calibrating the radiometers, and this problem is now corrected. Even so, there is still some timing problems in the software that occasionally shows up as missed events in the graphical user interface. Usually the problems can be circumvented simply by repeating the missed action.

There was also a rather regrettable software bug, which caused the Dicke radiometers to operate in total power mode. This bug was undiscovered for a few years, because the radiometer system still worked to some extent. The error was discovered after the new HF radiometer unit was built in 1996, and the large difference in their temperature stability was discovered. Once the location of the programming error was identified, the software was corrected and installed in the radiometer.

6.3. The LF amplifier

In general, the LF amplifier works as expected which is clearly shown in section 5. The linearity and step response of the entire radiometer chain is quite good, and therefore the LF amplifier can be assumed to have at least equal performance as the radiometer as a whole. These measurements were made for the entire radiometer chain and not only for the LF amplifier. This was done, because such a measurement would not be very informative as far as the radiometer receiver as a whole is concerned.

The operational amplifier type, XR-5533 from Exar, was chosen simply because the laboratory had some of them in stock, and the type was considered to be good enough for the purpose. The choice cannot be claimed to be a very educated one, but the circuit did work as expected and performed well enough. Consequently, there was no need to

look for a more suitable operational amplifier at the time. The LF amplifiers in the subsequently built 28.8, 36.5 and 94 GHz radiometer receivers use a OP37 [41] precision operational amplifier IC and a OP 467 [42] quad operational amplifier IC from Analog Devices instead.

The input amplifier impedance in the LF amplifier is designed to be in the order of 10 k-ohms, because the RF detector diode output impedance is assumed to be in the order of 1 k-ohm. This is, however, not known for a fact, but because the output impedance of the detector diode is linear as proven by the linearity test in chapter 5, any resulting errors can be fully compensated for by calibrating the radiometer receiver.

The instrumentation amplifier at the input should preferably also contain two buffer amplifiers at the input terminals in order to avoid the effect of the unknown impedance of the detector diode, but this is not a problem, as previously stated.

Some component values are slightly incorrect in the LF amplifier, because exact component values were not available when the amplifier boards were assembled. Most of these wrong components have now been corrected, but there may still be some incorrect resistance values installed in the LF amplifier circuit boards. These component value discrepancies may have caused minor artifacts in the oscilloscope graphs measured in chapter 5, but they are very small and they do not affect the radiometer data in any way because they are fully compensated for by the radiometer calibration procedure.

6.4. The Voltage-to-frequency converter

The voltage-to-frequency converter circuit is designed with simplicity in mind, and is not the best possible design when high precision is concerned. The linearity and step response tests of the entire radiometer receiver shows that the precision is sufficient, but for future designs, a different approach might be preferable. By adding a precision operational amplifier to the voltage-to-frequency converter circuit as described in the component data sheet, even higher precision can be achieved.

The dead time between integration cycles could have been avoided by using two integration counters and alternating between them. This double-buffered scheme would have required a double amount of counter hardware, and it was decided that it was not worth the extra complexity for such a small integration time loss.

The voltage-to-frequency converter is a precision component, and it is important that the associated components are of equal quality as the converter chip itself. One capacitor in the circuit was selected to be of a ceramic type by mistake, which greatly impaired the temperature stability of the voltage-to-frequency converter. This mistake went unnoticed for many years, because nobody in the HUTRAD team thought of the possibility. This erroneous component choice was detected only after careful research with a specially modified soldering iron, and the ceramic capacitor was replaced with a plastic capacitor, thus greatly improving the temperature stability of the radiometer.

6.5. Temperature measurement

The temperature measurement boards were originally equipped with switching isolation amplifiers, but the switching frequency suffered heavy interference from the VHF radio transmitter onboard the aircraft and had to be removed. A few small capacitors were also added in order to reduce the noise level and make the response time of the amplifier board slightly longer.

6.6. Temperature control

The temperature regulators work as required, even though they are not properly tuned in accordance with system control theory. Experimental tuning of the temperature regulator parameters turned out to be the easiest method and produced quite good results in most cases when done thoroughly.

The limited arithmetic precision of the control processor module proved to prevent fully optimal tuning of the P-term in the regulator loop because the arithmetic rounding error was affecting the setting. Nevertheless, all the regulators were successfully tuned to a stable state that was still able to drive the steady-state temperature error towards zero.

It is difficult to know which temperature channel measures which sensor, because the temperature channels are not named in any way. This is a problem, if the controlling sensor needs to be changed, because a proper decision needs knowledge of the sensor positions inside the radiometer receivers. These problems can be considered as missing features in the software.

6.7. Future developments

The HUTRAD radiometer system has now been in operation for more than ten years, and is beginning to show signs of old age. The oldest profiling radiometers are currently being evaluated in order to determine if it would be possible to refurbish some of them in order to improve their performance up to a more satisfying level, or if a total rebuild is necessary.

In any case, the current receivers have furnished valuable results that will be of the utmost importance for further radiometer development. The simplest thing to fix would be the problems with the software, but this could require re-writing most of it because it is based on old technology.

References.

[1] Panula-Ontto, E. Lentokäyttöinen radiometrijärjestelmä kaukokartoitukseen. Diplomityö. Teknillinen korkeakoulu. Espoo 1990.

[2] Jääskelainen, V. Hallikainen, M. Analysis Of Brightness Temperature Of Snow-covered Terrain. Geoscience and Remote Sensing Symposium. 1991. IGARSS '91. 'Remote Sensing: Global Monitoring for Earth Management'. International Volume: 4 3-6 Jun 1991. p. 2323-2327.

[3] Kurvonen, L. Lentokäyttöinen 94 GHz:n radiometri kaukokartoitukseen. Diplomityö. Teknillinen korkeakoulu. Espoo 1991.

[4] Menard, Y. Reynolds, M. The design of the ESA multiband imaging microwave radiometer MIMR, Digest 1991. International Geoscience Remote Sensing Symposium (IGARSS'91), Helsinki, Finland, p. 2359-2363.

[5] Tachi, K. Arai, K. Sato, Y. Advanced Microwave Scanning Radiometer (AMSR): Requirements and Preliminary Design Study. IEEE Transactions on Geoscience and Remote Sensing, Vol. 27. No. 2. March 1989. p. 177-183.

[6] Kemppinen, M. Pallonen, J. Hallikainen, M. 93 GHz Airborne Imaging Radiometer. IGARSS'94, Pasadena, USA, 8-12.8.1994. USA 1994, IEEE, p. 2243-2245.

[7] Pajuniemi, R. Roschier, M. Hallikainen, M. A Multisensor Remote Sensing Aircraft of the Helsinki University of Technology. URSI/Remote Sensing Club of Finland/IEEE XXIII Convention on Radio Science and Remote Sensing Symposium. Helsinki University of Technology, Report 35, 1998 p. 170-171.

[8] Mäkynen, M. Hallikainen, M. EMAC-95 HUT passive microwave radiometer measurements of baltic sea ice. URSI/Remote Sensing Club of Finland/IEEE XXIII Convention on Radio Science and Remote Sensing Symposium. Helsinki University of Technology, Report 35, 1998 p. 75-76.

[9] Cheng, David K. Field and wave electromagnetics, 2nd Ed. USA. 1989, Addison-Wesley Publishing company, 703 pages.

[10] Alonso, M. Finn, J. Fundamental university physics. Vol 1: Mechanics and Thermodynamics. Addison-Wesley, 1980 2nd ed.

[11] Tiuri, M. Radio Astronomy Receivers. Antennas and Propagation, IEEE Transactions on Antennas and Propagation, Volume 12, Issue 7, Dec 1964 p. 930-938.

[12] Dicke, R. H. The measurement of thermal radiation at microwave frequencies. Rev. Sci. Instr. Vol. 17. p. 268-275, 1946.

[13] K. E. Machin, M. Ryle, and D. D. Vonberg, "The design of an equipment for measuring small radio-frequency noise powers," Proc. IEE, vol. 99"; p. 127-134; May, 1952.

[14] Tirri, T. Lentokonekäyttöisen radiometrijärjestelmän tiedonkeruu- ja mittausohjelmisto. Diplomityö. Teknillinen korkeakoulu. Espoo. 1996.

[15] Boggs, D. Mogul, J. Kent, C. WRL Research Report 88/4. Measured Capacity of an Ethernet: Myths and Reality. Digital Western Research Laboratory. Palo Alto, California, USA. 1988

[16] Seifert, R. The Effect of Ethermet Behavior on Networks using High-Performance Workstations and Servers. Technical Report. Networks and Communications Consulting. Los Gatos. USA. 1995.

[17] Crynwr PC/TCP packet driver specifications.
http://www.crynwr.com/packet_driver.html, 1.2.2007
Ftp Software Inc. Wakefield, USA. 1989.

[18] Rautiainen, K. Lentokäyttöisen mikroaaltoradiometrin radiotaajuusosien suunnittelu ja toteutus. Diplomityö. Teknillinen korkeakoulu. Espoo. 1996.

[19] Lahtinen, J. Polarisaatioradiometrin kehittäminen kaukokartoitukseen. Diplomityö. Teknillinen korkeakoulu. Espoo. 1996.

[20] Pease, R. Versatile Monolithic V/Fs Can Compute as Well as Convert with High Accuracy. Linear Applications Handbook, Appendix D. pp 1247-1253. National Semiconductor. 1994.

[21] PC/104 Specification. PC/104 Embedded Consortium. 1992-2003.
http://www.pc104.org, 1.2.2007

[22] DM804 User's Manual. Real Time Devices, Inc. State College, USA. 1992.

[23] ANDI-MM Rev 1.1 Multipurpose Data Acqusition Card Technical Reference Manual. Ajeco Oy, Helsinki, Finland, 1991.

[24] AMD Am9513 System Timing Controller datasheet. Advanced Micro Devices. Sunnyvale, USA. 1980.

[25] http://en.wikipedia.org/wiki/Peltier-Seebeck_effect, 1.2.2007

[26] http://en.wikipedia.org/wiki/Platinum_resistance_thermometer, 1.2.2007

[27] ANDI-RTD Rev 1.1 Isolated Instrumentation Preamplifier Technical Reference Manual. Ajeco Oy, Helsinki, Finland, 1996.

[28] IEC-751 standard. Industrial platinum resistance thermometer sensors. 1983.

[29] http://en.wikipedia.org/wiki/Callendar-Van_Dusen_equation, 1.2.2007

[30] Lantto E. Kemppinen M. HUT/LST Kuvaavan radiometrin aktiivistabilointi, Raportti A13, Huhtikuu 1993, pages 27-29

[31] Discussion about technical note by Tuomo Auer, 13 may 1997

[32] Quinn, B. Almeroth K. IP Multicast Applications: Challenges and Solutions, RFC 3170, The Internet Engineering Task Force, 2001

[33] Mills, D. Network Time Protocol (NTP) General Overview, University of Delaware, 2004

[34] NE5533 Dual and single low noise op amp. Product specification, Philips Semiconductor, 1994.

[35] Millman, J. Microelectronics: Digital and Analog Circuit Systems, pp. 573-576, McGraw-Hill International Book Company, International Student Edition, 6th printing, 1984.

[36] Millman, J. Microelectronics: Digital and Analog Circuit Systems, pp. 569-573, McGraw-Hill International Book Company, International Student Edition, 6th printing, 1984.

[37] Widlar, R. Application Note 3: Drift Compensation Techniques for Integrated DC Amplifiers, National Semiconductor, Puerto Vallarta, Mexico, 1986.

[38] Millman, J. Microelectronics: Digital and Analog Circuit Systems, p. 576, McGraw-Hill International Book Company, International Student Edition, 6th printing, 1984.

[39] XR4151 Voltage-to-Frequency Converter. EXAR Corporation, Fremont, USA. 1997.

[40] LM 131A/LM 131/LM 231A/LM 231/LM 331A/LM 331 Precision Voltage-to-Frequency Converters. National Semiconductor. Arlington. USA. 1994.

[41] National Land Survey of Finland, lupanro 049/MYY/07, 1.2.2007

[42] Lemmetyinen, J. Kaukokartoitusradiometrin toiminnan arviointi ja jatkokehitys. Diplomityö. Teknillinen korkeakoulu. Espoo. 2004

[43] OP37 Low noise, Precision, High Speed Operational Amplifier data sheet rev.B, Analog Devices, 2002.

[44] OP467 Quad Precision, High Speed Operational Amplifier data sheet Rev.d, Analog Devices, 2001.